





Analysis of laminar and turbulent flows with turbomachinery, biotechnology and biomechanical applications

by

Gustaf Mårtensson

April 2006 Technical Reports from Royal Institute of Technology Department of Mechanics SE-100 44 Stockholm, Sweden







"gunderhaegg" — 2006/4/27 — 14:21 — page ii — #2



Typsatt i T
EX-Shop.

Akademisk avhandling som med tillstånd av Kungliga Tekniska Högskolan i Stockholm framlägges till offentlig granskning för avläggande av teknologie doktorsexamen fredagen den 5:e maj 2006 kl 13.30 i sal F2, Kungliga Tekniska Högskolan, Lindstedtsvägen 26, Stockholm.

© Gustaf Mårtensson 2006 Edita Norstedts, Stockholm 2006





"gunderhaegg" — 2006/4/27 — 14:21 — page iii — #3





Analysis of laminar and turbulent flows with turbomachinery, biotechnology and biomechanical applications

Gustaf Mårtensson

Department of Mechanics, Royal Institute of Technology (KTH) SE–100 44 Stockholm, Sweden

Abstract

The goal of this study was initially to gain a better understanding of the effects of rotation on turbulent flow in ducts. Knowledge concerning the influence of rotation on the structures of turbulence is of fundamental importance in many applications, e.g. centrifugal separators, turbines or cooling channels in rotating machinery, as well as meteorology and oceanography. Rapidly rotating duct flow is studied experimentally with rotation numbers in the interval [0, 1]. To achieve this, in combination with relatively high Reynolds numbers (5000 – 30000 based on the hydraulic radius), water was used as the working medium. The influence of the rotation on the pressure drop in the duct was investigated and suitable scalings of this quantity were studied. Due to questions that arose in the experimental study, two numerical studies were initiated. The first study probed the effect of rotation and geometrical configuration on the development length for turbulent flow, while the second comprised a direct numerical simulation of turbulent flow in a rotating duct. It is shown that while system rotation does not have a marked effect on the development length in a plane channel, the development length is substantially shortened in a duct.

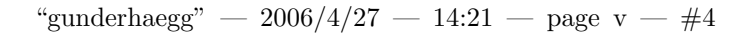
Additional systems subject to rotation or curvature effects were studied. The laminar flow of fluid in a rotating PCR-cone was analysed analytically and numerically to understand the increased mixing and temperature homogenization. The flow field in the cone was described and the increased mixing was due to a strong boundary layer flow incited by Coriolis and buoyancy effects. Comparisons of the numerical simulations with experiments yielded good results.

A study to quantify the flow of blood in cerebral malformations using three-dimensional videodensitometry was performed. Data from experiments with an idealized flow phantom, as well clinical pathologies, showed that the proposed methodology in conjunction with clinical injection protocols can yield mean flux data with an error less than 20%. Protocol improvements are proposed.

Descriptors: Turbulence, system rotation, Coriolis, duct, boundary layer development, direct numerical simulation, PCR, cone, buoyancy, hemodynamics, densitometry, cerebral malformation.











Preface

This thesis considers the study of laminar and turbulent flow in applications ranging from turbomachinery to those in the spheres of biomedical to biotechnology industries. The thesis is divided in two parts, where the first consists of an introduction to the topics of research at an accessible level for non-experts together with an overview and summary of the present contribution to the field of fluid mechanics. The second part consists of seven papers. A list of the papers and the contributions of different authors is included in the last chapter of Part 1

The seven papers in Part 2 are adjusted to comply with the present thesis format for consistency, but their content have not been altered in comparison with published versions.

Stockholm, April 2006 Gustaf Mårtensson









Contents

Preface	V
Part 1. Overview and summary	1
Chapter 1. Introduction	2
Chapter 2. Rotating channels and ducts	5
2.1. Introduction	5
2.2. Experiments in a rotating duct	7
2.3. Developing rotational flow	12
2.4. Direct numerical simulations	17
2.5. Summary	21
Chapter 3. Polymerase Chain Reaction	22
3.1. DNA	22
3.2. PCR	23
3.3. Improvements	27
3.4. Theory	29
3.5. Hypothetical flows	30
3.6. Calculations	31
3.7. Summary	35
Chapter 4. Blood flow in the brain	36
4.1. Introduction	36
4.2. What can go wrong?	36
4.3. How do we notice this?	38
4.4. How do we visualize the blood vessels?	39
4.5. What can be done?	40
4.6. Flow measurements	41
4.7. Materials and Methods	42
4.8. Experiments	46
4.9. Results	47
4.10. Summary	52
Chapter 5. Conclusions and outlook	53
5.1 Rotation	53







"gunderhaegg" — 2006/4/27 — 14:21 — page vii — #6



	CONTENTS	vii
5.2. Polymerase Chain Reaction5.3. Blood flow in the brain		54 54
Chapter 6. Papers and author contributions		55
5.2. Polymerase Chain Reaction 5.3. Blood flow in the brain hapter 6. Papers and author contributions cknowledgments bliography	57	
Bibliography		58
Part 2 Paners		63







"gunderhaegg" — 2006/4/27 — 14:21 — page 1 — #7

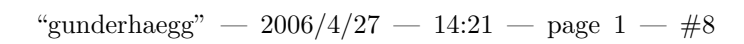


... all jävelskap börjar med jämförelse.

K.G. Hammar (f. 1943)











Part 1 Overview and summary









CHAPTER 1

Introduction

The conditions of discovery are rather elusive. When Sir Isaac Newton, arguably one of the most important natural scientists in history, wrote

"This most beautiful system of the sun, planets, and comets could only proceed from the counsel and dominion of an intelligent and powerful Being."

in his epic work of science *Philosophiae Naturalis Principia Mathematica*, he gave us an indication of the driving force of increased understanding over three hundred years ago. Newton believed that a clear understanding of nature would simultaneously reveal the inner workings of God.

In our secularized society, a search for God has perhaps been replaced by a quest for self-fulfillment or at least insatiable curiosity. This curiosity manifests itself in those troublesome questions, "Why?" and "How?".

These questions flutter around us constantly as we travel through life. A snowy day prompts us to ask, "Why does that snowflake have six *legs*?". With time on our hands, we can gripe, "Why do traffic jams suddenly appear?". With a sting of anxiety, a question gains footing in our minds, "How can this 175 ton airplane stay up in the air?". A bout of abstinence formulates the question, "Do piles of sand always have the same angle at the top?"

Although the value of attempting to answer these questions for the sake of pure understanding is evident and laudable, a more direct motive can be found in the development of society. The evolution of industry has been made possible by the ingenuity of men and women solving problems much like those posed above, but with some application in mind.

At first glance, it may seem that the need for understanding of fluid motion could be limited to classical areas such as aeronautics and shipbuilding. Where else could there be a need for such knowledge?

Look no further than to the automobiles that transport us to and fro. Not only is there the aerodynamic viewpoint of achieving a body form with low resistance, the internal combustion engine that drives the vehicle forward is a virtual cornucopia of fluid mechanics. Gas and air are injected, vapors are produced controlled explosions are performed regularly, pistons are lubricated, the list goes on and on (see Lumley (2001)).

The production of the gasoline that drives a majority of automobiles is also dependant on the physics of fluids. Not only do the oil companies have









1. INTRODUCTION

3



FIGURE 1.1. The wonders of nature that prompt us to ask "How?" and "Why?".

to try and optimize the extraction of oil from a porous media hundreds of feet beneath the surface of the earth (see Philip (1970)), but when they have succeeded, this mass of non-Newtonian fluid has to be pumped through various systems of co-annular and simple pipes en route to a refinery.

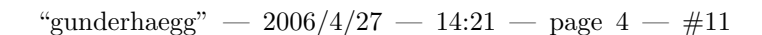
Fluid mechanics reaches in to our pockets in the increasing number of electronic devices that crave smaller batteries that last longer. The challenges of producing novel and efficient fuel cells include the effective transport of chemicals in intricately patterned channels, while optimizing reaction rates, see Becker (1972).

The scales that engineering operates at get smaller and smaller. Devices to pump and mix substances in for example the pharmaceutical and medical industries are being constructed at the micro- and nano-scale, see Stone et al. (2004). Controlling the motion of fluids at these scales press fluid mechanics to the threshold of statistical mechanics.

The body itself is a wonderful system of fluids. The heart very efficiently pumps blood throughout the circulatory system day after day. The wonders of the body are often first realized when we attempt to copy them. Much effort is being spent to understand the effect of blood flow on vessels, in order to assess treatment necessity and effectiveness, see Taylor and Draney (2004).









4 1. INTRODUCTION

Even those of us convinced of the necessity of a thorough physical understanding of our surroundings can be caught off guard by the areas where fluid mechanics has gained ground. Recent scientific presentations in the area of fluid mechanics have concerned the flight of bats, avalanche control and the impact of fluids research on homeland security in the United States (Settles (2006)).

This thesis concerns the study of the flow of fluids in applications ranging from turbomachinery to biomedical to biomechanical applications. Although the applications may initially seem disparate, they bear fundamental similarities in the manner which they may be described physically. The flows in rotating ducts and PCR cones and brain arteries are studied in order to gain understanding that can be used to optimize existing, as well as develop new, industrial devices. Even if the basic goals of this work have been to produce palpable results, the driving force has been those two questions presented earlier, "How?" and "Why?".









CHAPTER 2

Rotating channels and ducts

The study of fluid flow in non-inertial frames of reference is of great interest to both academia and industry. Industrial applications, such as centrifugal separators, turbines and radial compressor impellers are all systems that incorporate rotating bodies of fluid. It is known that Coriolis effects in rotating flows are of primary importance not only for mean flow quantities, such as bulk velocity, but also for turbulence intensities and structures. The ability to accurately model these effects offers the possibility of increasing device performance, while shortening the time for expensive prototype development. In order to assess the accuracy of turbulence models that are developed, both carefully collected experimental and numerical data from well-defined test cases are needed. In the following studies concerning experimental measurements and numerical simulations are presented that elucidate various aspects of the effect of rotation on the flow in channels and ducts.

2.1. Introduction

The equations of motion that govern the instantaneous flow of an incompressible fluid in a rotating frame of reference can be expressed as follows,

$$\frac{\partial u_i}{\partial t} + \frac{\partial}{\partial x_j}(u_i u_j) = -\frac{\partial p^*}{\partial x_i} + \frac{1}{\text{Re}} \frac{\partial^2 u_i}{\partial x_j \partial x_j} + 2\text{Ro}\,\varepsilon_{ijk} u_j \Omega_k$$
 (2.1)

and

$$\frac{\partial u_j}{\partial x_j} = 0 \quad , \tag{2.2}$$

where u_i denotes the instantaneous velocity in the x_i -direction, Ω_i is the rotation in the same direction and ε_{ijk} is the Levi-Civita symbol. The term p^* , known as the reduced mean static pressure, conveniently incorporates the centrifugal pressure term and is expressed as

$$p^* = p - \frac{1}{2}\rho\Omega^2 \vec{r}_{\perp}^2$$
 , (2.3)

where \vec{r}_{\perp} is the position vector normal for the axis of rotation to a given mass element.

The equations have been non-dimensionalized by the bulk velocity, U_b , and the hydraulic diameter, d_h , defined as,









6 2. ROTATING CHANNELS AND DUCTS

$$U_b = \frac{Q}{w \cdot h}, \qquad d_h = \frac{2(w \cdot h)}{(w+h)} . \tag{2.4}$$

Here Q denotes the volume flow, while w and h are the width and the height of the duct, respectively. The Reynolds number and the Rotation number become $\mathrm{Re} = U_b d_h/\nu$ and $\mathrm{Ro} = \Omega d_h/U_b$, respectively. The Ekman number can be formed from the Reynolds and the Rotation number, as $\mathrm{E} = 1/(\mathrm{Re} \cdot \mathrm{Ro})$. The inverse of the Rotation number is often referred to as the Rossby number,

The Coriolis force has a significant effect on the dynamics of the flow, even at low rotation rates. The Coriolis effect on the flow is two-fold in a turbulent duct flow. The Coriolis force sets up a pressure gradient in the y-direction, so that the main balance in the y-component of equation (2.1) in the central region of the flow is given by

$$\frac{\partial p^*}{\partial y} = -2\operatorname{Ro} u \quad . \tag{2.5}$$

In a plane channel with a homogeneous z-direction, this results in a pressure field that causes a for rotational flows characteristic tilted velocity profile. In a duct with finite extension in the z-direction, the wall boundary conditions give a spanwise variation of the streamwise velocity that in turn yields a spanwise pressure gradient and a resulting secondary flow in the cross-stream plane. Near the z-boundaries, where the axial velocity, and hence the Coriolis force, is smaller than in the center of the duct, the pressure gradient in equation (2.5) will drive a flow in the positive y-direction. The resulting secondary flow is illustrated schematically in Figure 2.1.

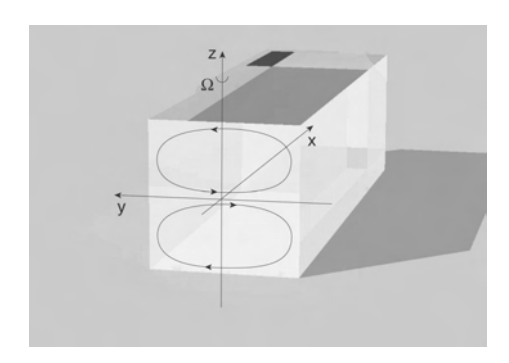


FIGURE 2.1. The secondary flow in a rotating square duct.

Near the z-boundaries, we have a turbulent counterpart to Ekman layers. We may consider the region close to the y-boundaries as a turbulent counterpart to the Stewartson layers. We should keep in mind that in the present turbulent case, there is an influence of the Reynolds stresses on the secondary flow.









7

2.2. EXPERIMENTS IN A ROTATING DUCT

The laminar Ekman and Stewartson layer thicknesses scale as $E^{\frac{1}{2}}$ and $E^{\frac{1}{3}}$ or on dimensional form, $\delta_{E} \sim (\nu/\Omega)^{\frac{1}{2}}$, $\delta_{S} \sim (\nu d_{h}/\Omega)^{\frac{1}{3}}$. There can also exist secondary Stewartson layers whose thicknesses are proportional to $E^{\frac{1}{4}}$.

In requiring the vertical Ekman layers to carry the same mass flux as the horizontal Stewartson layers, it is obvious that the major contribution to the total wall shear, and thereby flow resistance, originates from the Ekman layers in this range of Rotation numbers. The situation is of course modified in a turbulent case, but it is reasonable to expect that the increase in friction coefficient will scale approximately with the width of the duct, rather than with the hydraulic diameter.

2.2. Experiments in a rotating duct

Rotating ducts, or analogous details, such as bends and curves, are present in almost all mechanical systems where some kind of fluid is transported from one place to another. This fact has made the study of the effect of rotation or curvature on the flow of fluid very common. Interest in the specific application of fluid separators prompted by a collaboration with Alfa Laval AB, led to a focus on rotational effects on turbulent flow in the rectangular ducts. A straight rectangular duct is an idealization of the distribution channels that can be found in any industrial centrifugal separator, see Figure 2.2.

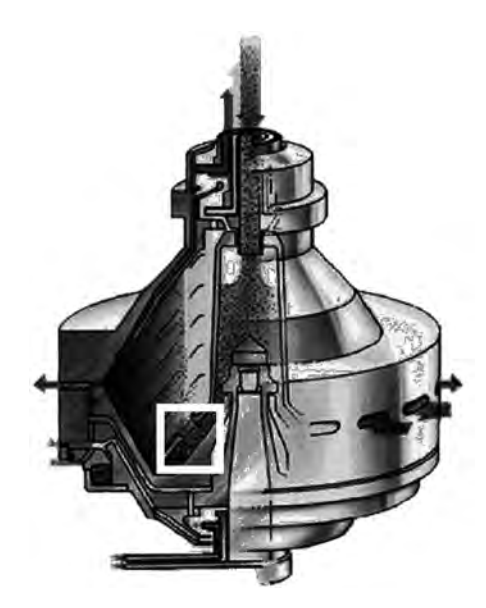


FIGURE 2.2. An illustration of a separator. The distribution channels that lead fluid into the separator are marked by the white square, while separation occurs between the conical plates at the center of the device.





"gunderhaegg" — 2006/4/27 — 14:21 — page 8 — #15





8 2. ROTATING CHANNELS AND DUCTS

Rotating channels and ducts have been studied extensively over the years. Experimental studies of this case have been performed over at least five decades, see Dobner (1959); Johnston et al. (1972); Smirnov (1983). These experiments have spread much light on the very powerful interaction of rotational forces and fluid flow. These effects include the stabilization and destabilization of opposing vertical sides of the duct/channel, skewing of the streamwise velocity profile, and the introduction of a powerful symmetry breaking secondary flow in the case of a rotating duct.

The rotation rates used in centrifugal separators are extremely high, in excess of 10^4 rpm. The lack of experimental studies for turbulent flow in this parameter region prompted a new experimental study of this case. The experimental setup is illustrated schematically in Figure 2.3. The overall channel length was 490 mm, giving a ratio of length to hydraulic diameter of between 30-47, depending on the choice of duct. The inlet length required can be shortened by introducing disturbances at the inlet.

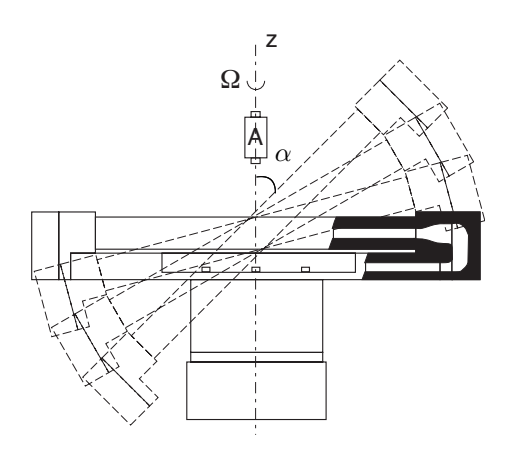


Figure 2.3. Schematic of the experimental apparatus. The pressure transducer is labeled $\bf A$.

In order to obtain high Rotation numbers in combination with high Reynolds numbers, water was chosen as flow medium. The highest rotation rate used in the present investigation was approximately 25 rad/s.

To achieve a rotation vector that is not perpendicular to the direction of the main flow, a construction with four interchangeable middle sections was used. The angle between the axis of rotation and the longitudinal axis could in this way be altered in four discrete steps (90°, 75°, 60° and 45°). The construction was machined from solid aluminium in order to obtain the rigidity to withstand the dynamic forces due to the asymmetry of the construction.

A total of five different duct geometries were used during the experiments, see table 2.1, giving a total of twenty (20) different possible configurations, for each combination of Reynolds and Rotation numbers.









9

2.2. EXPERIMENTS IN A ROTATING DUCT

Re	5000 - 3	0000					
Ro	0 - 1.0						
α	45°	60°	75°	90°			
A	1/1	2/3	3/2	1/3	3/1		
$w \times h$	15×15	14×21	21×14	7×21	21×7		

Table 2.1. Parameter range of the experiment (A = w/h, w) and h in millimeters).

Pressure holes with a diameter of 0.5 mm were placed at 10 cm intervals along the duct centerline. The differential pressure transducer was mounted on the axis of rotation, see Figure 2.3. Extensive information concerning the experiments can be found in Papers 1 and 4.

2.2.1. Rectangular duct

From previous experimental studies, it is known that the pressure drop, or friction coefficient, in a rotating duct is larger than in a stationary duct. In order to study this further, the flow in a number of ducts of varying rectangular configurations was studied. For the rotating duct, we may assume that the friction coefficient should be a function of the Rotation number, as well as the Reynolds number, $\lambda = \lambda(\text{Re, Ro})$.

If the normalized friction coefficient is plotted versus the parameters Ro_h and Ro_w , where the indices h and w imply that the characteristic lengths were chosen as the height and the width of the duct geometry, respectively, a monotonic increase of the friction factor is observed with increasing Rotation number. A far better collapse of the data is observed for those plotted versus Ro_w , implying that the width of the channel is important length scale of for this flow. This observation supports a view that the increase in pressure drop in the rotating duct is controlled by the Ekman layer's influence along the length of the channel

2.2.2. Tilted duct

To further probe the importance of the geometrical configuration of the duct, and with it the influence of the induced boundary layers, the case of the tilted duct was studied. The channel was tilted 45° around its longitudinal axis. If the square duct is tilted in this way, the friction coefficient increases more rapidly with the rotation rate, see Figure 2.5 a).

One possible explanation of this is that instead of the standard configuration of two Stewartson layers and two Ekman layers of the untilted case, four Ekman layers are formed on the walls of the tilted duct, see Figure 2.6. This is believed to be a geometric effect, since in this case, the rotation vector has a component normal to each of the walls, thereby generating Ekman layer-like boundary layers.









10 2. ROTATING CHANNELS AND DUCTS

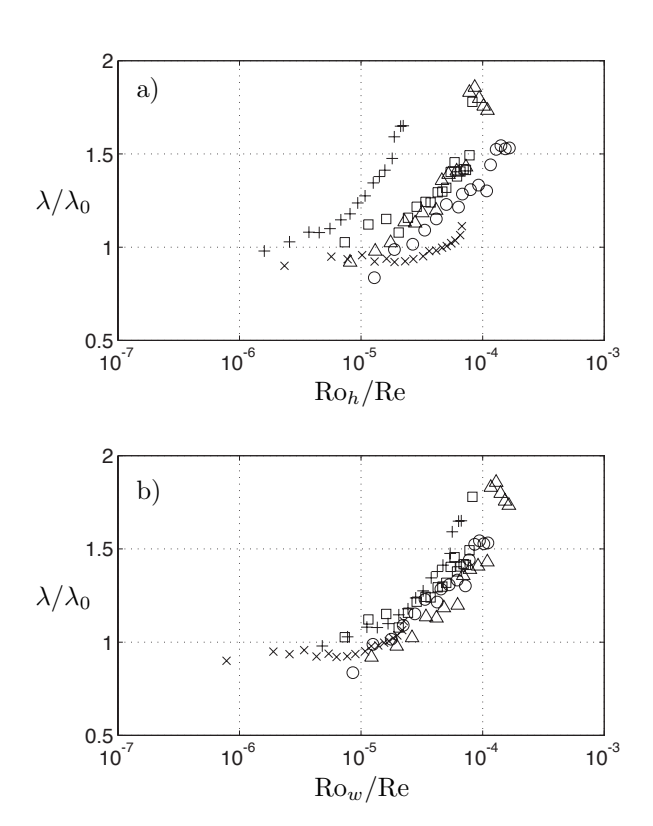


FIGURE 2.4. Normalized friction loss coefficient versus the Rotation number for Re = 10000. In a), the characteristic length for the Rotation number is chosen as the height of the channel, while in b), this length is chosen as the width of the channel. $(w \times h) \square : 15 \times 15, \times : 7 \times 21, +: 21 \times 7, \circ : 14 \times 21, \triangle : 21 \times 14$.

The wall shear stress in a boundary layer may be taken to be proportional to the inverse of the boundary layer thickness.

$$\tau_w = \mu \frac{dU}{dy} \sim \frac{1}{\delta} \quad . \tag{2.6}$$

Using the scalings of the Ekman layers mentioned earlier, the wall shear stress of the Ekman layers in the tilted configuration can be expressed as

$$\tau_w \sim \left(\frac{d^2 \Omega_\alpha}{\mu}\right)^{\frac{1}{2}} \tag{2.7}$$









11

2.2. EXPERIMENTS IN A ROTATING DUCT

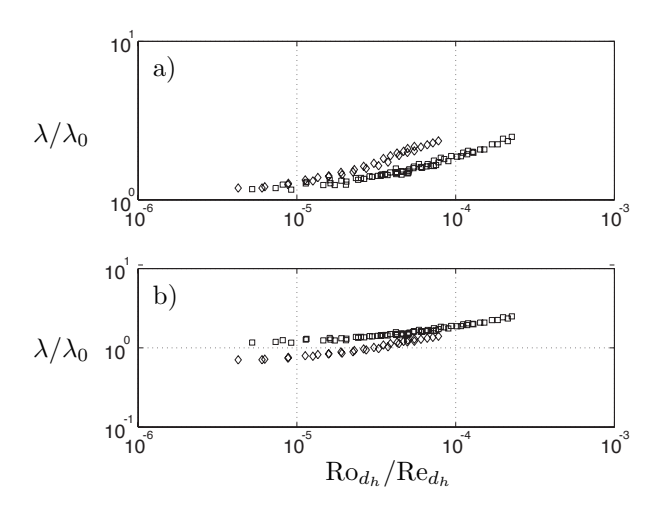


FIGURE 2.5. Normalized friction coefficient for a duct tilted by 45° (\diamond) and a non-tilted duct (\square). In a), the the normalized friction coefficient has been plotted as measured in the two cases, while in b), the data from the tilted channel has been adjusted by a factor $2/\sqrt[4]{2}$.

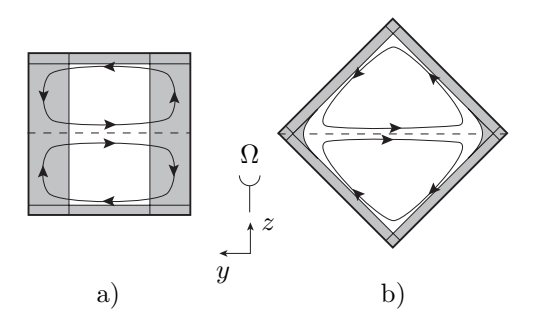


FIGURE 2.6. By tilting the duct 45° around the streamwise axis, four Ekman layers may be formed, instead of two in the case of a non-tilted channel. A probable appearance of the secondary flow in these two geometrical configurations is also included.

The rotation term Ω_{α} is the wall-normal component of the system rotation vector. Using the angle notation in Figure 2.6, we may rewrite equation (2.7) as









12 2. ROTATING CHANNELS AND DUCTS

$$\tau_w \sim \left(\frac{d^2\Omega \sin \alpha}{\mu}\right)^{\frac{1}{2}}$$
(2.8)

In the case at hand, the duct was rotated 45 degrees, a scaling factor of $\frac{1}{2}\sqrt[4]{2}$ between the tilted and non-tilted cases is obtained. This factor is dependent on the assumption that in the non-tilted case, the two Ekman layers are the dominant contributors to the total pressure drop in the duct. However, the large corner regions in the tilted case may also be of significant influence.

The collapse of data is good if the above scaling is applied to the available data, see Figure 2.5. The agreement is better for higher rotation rates which is in line with the reasoning above.

2.3. Developing rotational flow

The experiments described in Section 2.2 provided interesting insights into rotating turbulent flow at very high rates of rotation. They also gave rise to a number of questions that deserved further attention. One of the more important and poorly understood issues concerned the length of the experimental duct.

Although a majority of industrial applications operate in the regime of developing flows, the goal of the experiments was to study the effect of rotation on the idealized case of fully developed turbulent flow in a rectangular duct. Physical restrictions limited the length of the experimental duct to 490 mm, producing a ratio of length to hydraulic diameter of between 30-47, depending on the choice of duct. It is customary to try to achieve a length to height ratio of at least 50 in experiments on pipe or duct flow to guarantee a fully developed profile. A length to height ratio of 32 was used by Johnston et al. (1972) and assumed to be adequate for the pressure measurements performed. Due to the limited length of the experimental set-up, it is natural to question whether the flow in the measurement region was fully developed.

Numerical studies of rotating turbulent flow are common, see for example Wallin and Johansson (2002); Sjögren and Johansson (2000); Pettersson and Andersson (2003). Specific studies concerning the effect of rotation on development of flow quantities are more scarce. A numerical study concerning developing turbulent flow in a rotating plane channel was performed by Nilsen and Andersson (1994). An algebraic second-moment closure with rotation stress-producing terms embodied was used to simulate the flow. Nilsen found that the turbulent boundary layers had merged after approximately 20 channel widths, while the flow could be deemed fully-developed after less than 40 channel widths at a rotation number of 0.12.

Dutzler et al. (2000) performed a numerical study of the development of a turbulent channel flow using a second-moment closure by Ristorcelli et al. (1995). The experimental conditions in the study of the experimental study of Koyama and Ohuchi (1985) were mimicked with great care to enable comparison with that data set. The calculations were carried out for two cases, one





"gunderhaegg" — 2006/4/27 — 14:21 — page 13 — #20





13

2.3. DEVELOPING ROTATIONAL FLOW

non-rotating and one rotating at $\Omega=10\pi$ rad/s, the rotation number based on half-width, H, being Ro = 0 and 0.25. Dutzler's results show good agreement with the experimental findings, although the growth of the boundary layers was somewhat over-predicted. The calculations predicted a merging of the boundary layers at x/H=25, while fully developed flow conditions were established beyond 75 H. Dutzler states that the over-predicted boundary layer development may be attributed to the lack of horizontal end-walls due to the two-dimensionality assumption in the calculations.

In summary, it appears that the understanding of the effects of rotation on the development length of turbulent channel and duct flow is still far from complete. Calculations have shown little difference between the development lengths of rotating and non-rotating flows (Dutzler et al. (2000) for example), while experimental studies of channel-like flow have claimed that the entry length for rotating flows is markedly shorter, see Johnston et al. (1972).

A numerical study was initiated not only to probe the full development of turbulent flow quantities in a rotating channel and duct and obtain a more thorough understanding of the effect of rotation on turbulent flow, but also allow for a better critical evaluation of experimental measurements in systems that are inherently limited in length.

2.3.1. Simulation

The numerical simulations were carried out using the package EDGE developed at the Swedish Defence Research Agency (FOI). EDGE is a flow solver for unstructured grids of arbitrary elements. The solver is based on an edge-based formulation and uses a node-centered finite-volume technique to solve the compressible Reynolds Averaged Navier-Stokes equations. The control volumes are non-overlapping and are formed by a dual grid obtained from the control surfaces for each edge. A Runge-Kutta time integration is implemented to integrate the governing equations explicitly towards steady state. The techniques of agglomeration multi-grid and implicit residual smoothing are used to accelerate convergence.

Calculations have been performed for incompressible, developing channel and duct flows. The geometries used in the calculations are shown schematically in Figure 2.7. The dimensions of the duct and channel were chosen so as to facilitate comparisons with the experiments of Mårtensson et al. (2002).

The calculation domain used for the duct was $201 \times 97 \times 49$ grid points in the x,y and z-directions, corresponding to actual dimensions of $2000 \times 15 \times 7.5$ mm. The duct was thus 130 duct widths long. Only half of the domain was calculated due to the symmetrical nature of the flow. Since the channel flow is a two dimensional flow, the domain was reduced in the z-direction to three nodes and periodic boundary conditions implemented on the upper and lower surfaces.

A no-slip condition is enforced on the walls of the duct and channel. At the inlet and outlet of the duct/channel, a total temperature and pressure condition is imposed.









14 2. ROTATING CHANNELS AND DUCTS

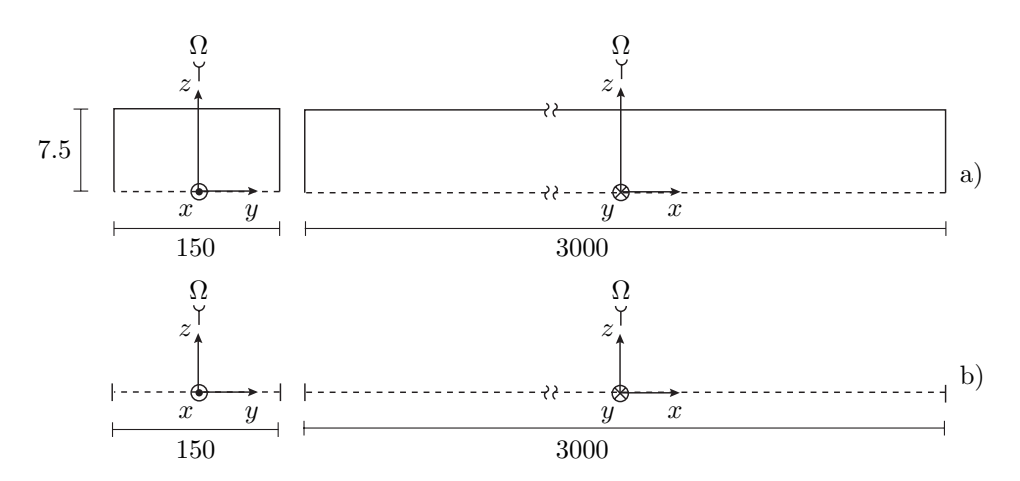


FIGURE 2.7. The two flow cases at hand, a) square duct and b) plane channel flow. The flow is in the x-direction. The pressure, or destabilized, side of the channel is situated on the negative y-axis, while the suction, or stabilized, side is on the positive y-axis. All dimensions are in millimeters.

An explicit algebraic Reynolds stress model (EARSM) that compensates for curvature effects (Wallin and Johansson (2002)) was used to model the viscous terms in the turbulent flow.

Calculations were carried out for six rotation rates, corresponding to Ro = 0, 0.048, 0.095, 0.19, 0.38 and 0.76. The Reynolds number based on the channel/duct width for the flows was approximately $Re_d = 6000$.

2.3.2. Results

The main effort in this study is to probe the effect of rotation on the development length of turbulent flow in a duct with a square cross section. The presented results will show that rotation has a dramatic effect on the development of turbulent quantities of the flow in a rotating square duct.

The reliability of the predictions made in this study are dependant on the ability of the turbulence model chosen to mimic the mechanisms contained in this intricate flow. In Figure 2.8, a contour and quiver plot are combined to visualize the three velocity components for the case of duct flow at Ro=0.38 at x=0.5 m. The flow exhibits the many characteristic qualities expected from rotating duct flow, such as, thin Ekman layers on the horizontal surfaces, a symmetric two-cell secondary flow, stabilized and destabilized vertical sides and a shifted mean velocity profile. The characteristic damping of motion in the direction parallel to the axis of rotation, the z-direction in this case, is also noticed in the stratification of the core of the flow.

A number of different quantities may be used to assess the degree of development of the flow. These quantities, whether they be mean flow velocities,









15

2.3. DEVELOPING ROTATIONAL FLOW

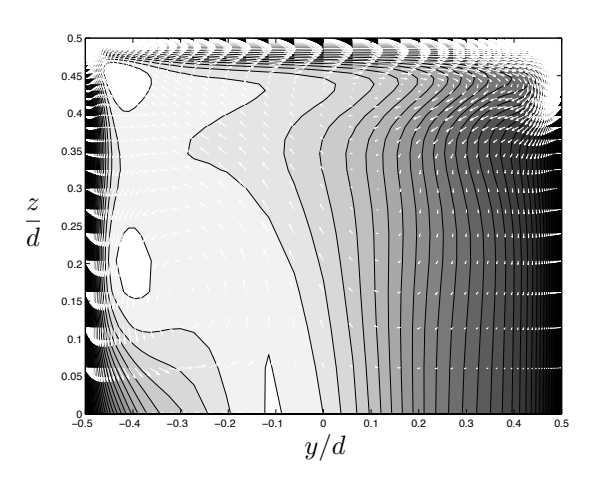


FIGURE 2.8. Contour plot for u and vector field of the secondary flow, v and w, for Ro = 0.38.

Reynolds stresses or averaged wall shear velocities, will impart understanding concerning the processes present during flow development. In Figure 2.9, a local wall shear velocity u_{τ} at the center of the respective sides of the duct/channel is plotted versus the streamwise distance x. The first observation made is perhaps the dramatic introduction of the Ekman-like boundary layer in the duct configuration, with a u_{τ} that is approximately five times that for either the stabilized or destabilized sides of the channel and duct. This supports the conclusion from the experiments performed and described in Section 2.2 that the pressure drop in a rotating duct is dominated by the thin Ekman-like layers on the horizontal surfaces.

Additional observations can be made from Figure 2.9. If the development lengths for u_{τ}/U_b on the vertical sides of the channel and duct are compared, it is seen that the duct's is noticeably shorter. The development length for u_{τ}/U_b in the Ekman-layer in the duct is longer than that for the vertical surfaces in the square duct. The development of u_{τ}/U_b in the Ekman layer is intimately tied to the secondary flow induced by rotation. This interaction is also involved in the very quick development of u_{τ} in the duct.

To clarify the effect of rotation on the flow in the duct configuration, u_{τ}/U_b for the two rotation numbers Ro = 0 and 0.38 are plotted in Figure 2.10. It is clear that the induced secondary flow has a dramatic effect on the development of the shear levels on the respective sides of the duct.

Although the trend of a shorter development length for the duct with respect to a channel is consistent for the other flow quantities evaluated, it is interesting to observe that their actual development lengths vary considerably. The development of the secondary flow is very rapid, while the development of streamwise velocity profiles seems to lag somewhat behind shear velocities.









16 2. ROTATING CHANNELS AND DUCTS

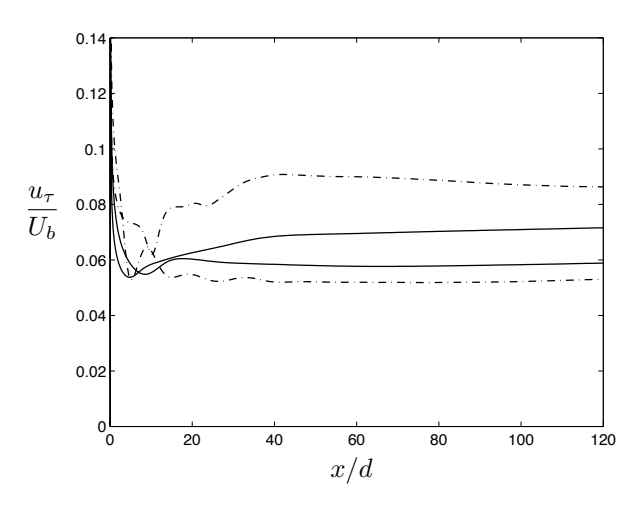


FIGURE 2.9. The local wall shear velocity u_{τ}/U_b at the middle of the sides of the channel/duct as a function of the streamwise direction x for Ro = 0.38 for the channel (—) and the duct (—) on the suction, pressure and Ekman sides.

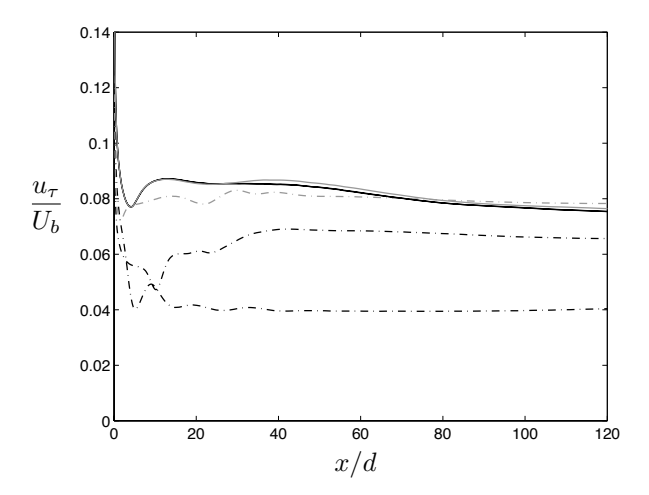


FIGURE 2.10. The local shear velocity u_{τ}/U_b at the middle of the sides of the duct as a function of the streamwise direction x for Ro = 0 (—) and 0.38 (—) for the suction (lower black), pressure (upper black) and Ekman (grey) side of the duct.





"gunderhaegg" — 2006/4/27 — 14:21 — page 17 — #24





17

2.4. DIRECT NUMERICAL SIMULATIONS

The performed simulations support the assumption that rotation will decrease the development length necessary for a turbulent flow in a rotating duct, put forth by among others Dobner (1959) and Johnston et al. (1972). Although this is true, it is important to understand the development length necessary for the flow quantity that is to be measured. In the case of Johnston et al. (1972) and Mårtensson et al. (2002), the relatively short experimental ducts will probably not have adverse effects on their measurements of shear stress and pressure, respectively.

Further details concerning the numerical calculations and practical implications of these theories are available in Paper 2.

2.4. Direct numerical simulations

In the previous experimental and modelling efforts, we have been at the hands of uncertainty. In the experimental case, the question of development lengths for rotational flow limit our ability to draw far-reaching conclusions. The modelling studies performed to attempt to answer these questions, instead are based on the approximations inherent to the turbulence models used in the simulations.

2.4.1. The simulation

A DNS of turbulent flow in a square duct of width and height w and length ℓ , rotating along an axis normal to the direction of the mean flow, is carried out, see Figure 2.11. The flow field was assumed to be fully developed and periodic boundary conditions in the flow direction were therefore used. The mass flow was kept constant by adjusting a variable pressure gradient.

The equations of motion (eqs. 2.1 and 2.2) are discretized by means of a second-order accurate finite volume method on a staggered grid. A second-order Adams-Bashforth scheme was used for the time integration of advective and diffusive terms. For the solution of the Poisson equation for the pressure we apply a Fast Fourier Transform in the periodic direction and cyclic reduction solver for the remaining directions.

The computation was carried out for a domain of size $9.4 \times 1 \times 1$ in the x, y, and z direction, respectively. In order to resolve the boundary layers of the duct flow which become increasingly thin with increased rotation number, a criterion of fifteen grid points within the boundary layer has been set. The grid points are uniformly distributed in the x-direction, while the grid was refined exponentially towards the side walls of the duct in the y and z directions. The average grid spacing in wall units in the streamwise direction is $\Delta x^+ = \Delta x u_\tau / \nu \approx 13$, while, $\Delta y^+ = \Delta z^+ \approx 3$.

Simulations have been performed for a set of rotation numbers between 0 and 0.77, where the rotation number is Ro = $\Omega w/U$, where Ω is the rate of rotation, U is the bulk flow velocity and w is the width of the duct. The Reynolds number was chosen to be Re = Uw/ν = 4400, where ν is the kinematic viscosity, in order to facilitate validation comparisons with the work of Gavrilakis (1992) for turbulent flow in a stationary duct. A comparison of major flow features for the two simulations showed good agreement.









18 2. ROTATING CHANNELS AND DUCTS

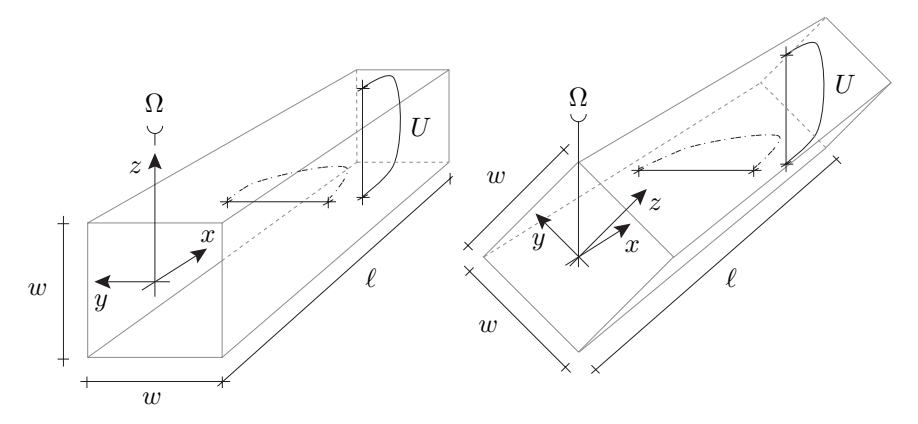


FIGURE 2.11. A schematic of the two simulated flow configurations for the rotating duct. The rotation vector $\vec{\Omega}$ in the tilted duct (to the right in the figure) is at a 45 degree angle with reference to the y and z axes. The asymmetric velocity profile $(-\cdot)$ in the xy-plane is shown, as well as the symmetric velocity profile (-) in the xz-plane.

2.4.2. Mean flow

In the velocity profiles of the mean streamwise flow of the present simulations, see Figure 2.12, an overview of the effects of rotation on turbulent flow may be obtained. The interaction of the inclined core region of the flow and the secondary flow can readily be observed. The velocity profiles in the xy-plane show a clear 2Ω region on the destabilized side of the duct (y=0), while exhibiting an increasingly laminar-like profile on the stabilized side (y=1). This channel-like region is steadily decreased as rotation rate increases and the secondary flow increasingly dominates the flow.

It is also noticed that a vertical elongation of the curves in Figure 2.12 b) is evident for increasing rotation number implying that the flow becomes more uniform in the z-direction, also producing the very thin boundary layers on the horizontal surfaces. This is not surprising considering the tendency towards a columnar Taylor-Proudman flow of reduced dimensionality that is characteristic for rotational flows

2.4.3. Boundary layers

By studying the flow fields made available through the simulations, it is clear that there are three distinct types of boundary layers present, the horizontal Ekman layers and the vertical boundary layers on the stabilized and destabilized sides of the duct. Theory for laminar rotational flow predicts a thickness for the Ekman layers that scales as $1/\sqrt{\text{Ro}}$, while the vertical Stewartson layers follow a $1/\sqrt[3]{\text{Ro}}$ or $1/\sqrt[4]{\text{Ro}}$ scaling, see Greenspan (1968).









19

2.4. DIRECT NUMERICAL SIMULATIONS

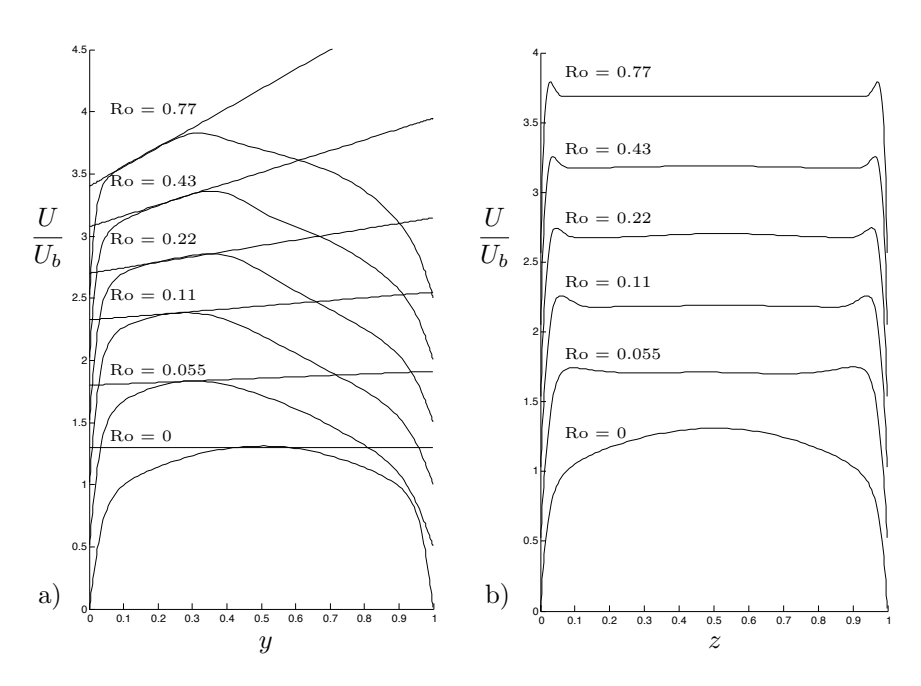


FIGURE 2.12. Velocity profiles of $U_{\rm mean}/U_b$ in a) the xy-plane at z=0.5 and b) xz-plane at y=0.5 for Ro = 0, 0.055, 0.11, 0.22, 0.43 and 0.77 from bottom to top. In a) straight lines with a slope of 2Ω are plotted.

In accordance with laminar theory, the thickness of the Ekman layer-like boundary layer was shown to follow the $1/\sqrt{\text{Ro}}$ -scaling as can be observed in Figure 2.13.

The experimental study described in Section 2.2 provided evidence that the friction coefficient scales with the width of the duct. The DNS shows that the horizontal Ekman layers are markedly thinner than the vertical Stewartson-like layers resulting in a dominating contribution to the pressure drop from the horizontal Ekman layers, supporting the width of the duct as the primary scaling length.

2.4.4. Tilted duct

The case of a duct that has been tilted around the direction of the mean flow was studied, see Figure 2.11, in response to the experimental results presented in Section 2.2.2 that showed an increase in friction factor for the tilted configuration. Simulations of the same case show many of the same characteristic flow qualities as the non-tilted case. The flow is clearly symmetric with respect to the spanwise axis normal to the axis of rotation, see Figure 2.14. The mean streamwise flow is skewed towards the destabilized side of the duct, which is a









20 2. ROTATING CHANNELS AND DUCTS

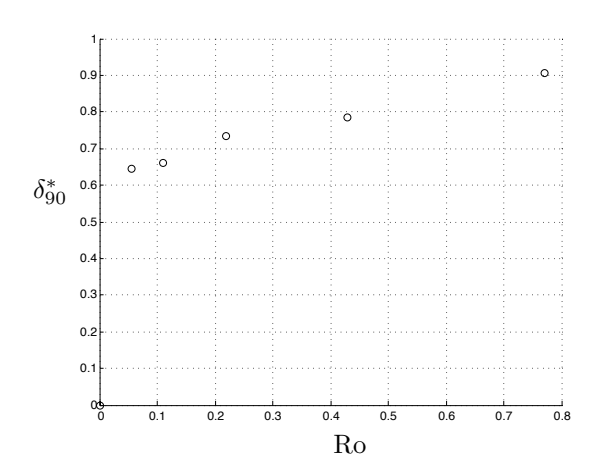


FIGURE 2.13. The scaled boundary layer thickness $\delta_{90}^* = \delta_{90}/\sqrt{\nu/\Omega}$ of the horizontal Ekman layer for the rotation numbers Ro = 0, 0.055, 0.11, 0.22, 0.43, and 0.77.

corner in this flow scenario. Two secondary circulatory cells are also formed in this duct configuration.

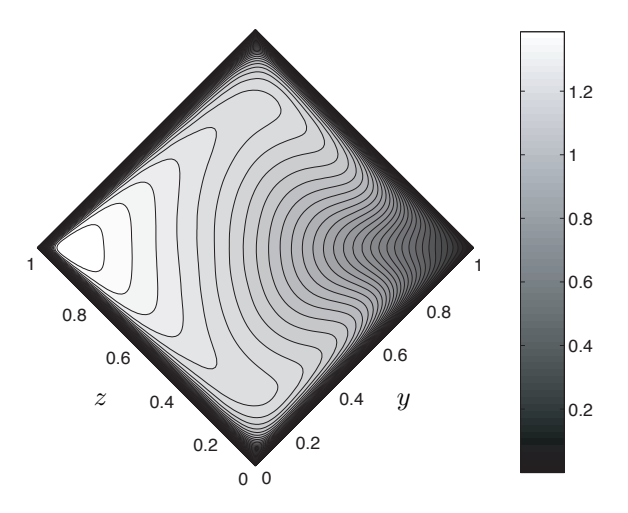


FIGURE 2.14. Plot of $U_{\rm mean}/U_b$ -contours tilted configuration ($\alpha=45^\circ$) for Ro = 0.055.





"gunderhaegg" — 2006/4/27 — 14:21 — page 21 — #28





2.5. SUMMARY

21

A comparison of the streamwise flow resistance for the tilted and non-tilted configuration shows a decrease of approximately 10% of the integrated shear stress in the tilted case. This supports the modelling results of Pettersson and Andersson (2003), but contradicts the experimental findings of Mårtensson et al. (2002). Although Ekman-like boundary layers develop on all four sides of the duct in the tilted configuration, they do not extend along the surfaces to the same extent as in the non-tilted case. The two surfaces on the unstable side of the duct have boundary layers that increase linearly in thickness towards the center of the duct. The flow on the stabilized side of the duct exhibit a thicker circulation zone near the apex of the duct on that side. The Ekman-like behaviour of the boundary layer is thus effective on, at most, half of the surface, see Figure 2.14. This behaviour of the Ekman layers would entail a slight decrease of the pressure drop in the duct in the tilted case.

Further details and results from the DNS are available in Paper 3.

2.5. Summary

In order to better understand the various effects of rotation on turbulent flow in a rectangular duct, experiments and numerical simulations have been performed. The experiments were performed for high rotation and flow rates and showed that the pressure drop in a rotating duct is primarily dependant on the magnitude of the rotation normal to the streamwise component of the flow, and concentrated to the thin Ekman-like boundary layers on the horizontal surfaces. The importance of the Ekman layers was supported in both the EARSM simulations and calculations using DNS.

The importance of the boundary layer configuration was evident when the experimental duct was tilted 45 degrees relative to streamwise direction. An intriguing result was obtained in an increase in friction factor for the tilted configuration. A boundary layer system consisting of four tilted Ekman layers was proposed.

Questions concerning the length of the experimental set-up prompted the EARSM simulations an an attempt to understand how the development length in channels and ducts was affected by the introduction of rotation. The simulations exhibited clearly a shortening of the necessary length for development of averaged flow quantities when the system was subjected to rotation.

The need for fundamental understanding of rotational effects on confined flow incited a DNS study of turbulent flow in a rotating duct. The simulations support a majority of the conclusions from the previous experimental and numerical studies. The exception concerns the resistance in a titled square duct configuration, described earlier, where the DNS predicts a decrease in pressure drop, in conflict with the experimental results. The simulations suggest that the proposed boundary layer system with four tilted Ekman layer must be adjusted to compensate for the boundary layer's effective area on each of the duct's surfaces.









CHAPTER 3

Polymerase Chain Reaction

The applications of fluid mechanics are many and widespread. The tried and true applications of fluid mechanics on aeronautical and process industries have been supplemented with among others the biomedical and pharmaceutical industries. An understanding of the physics of fluid flow has been recognized to be of importance in mixing processes at macro- and micro-scopic scales, as well as the control of flow in microscopic analysis devices.

One such biomedical process that has shown not only industrial, but also fundamental academic, interest focuses on the amplification of DNA sequences using Polymerase Chain Reaction (PCR).

3.1. DNA

Ever since the early 1950's, when the structure of DNA (deoxyribonucleic acid) was determined by James Watson and Francis Crick (Watson and Crick (1953)), it has been recognized that DNA holds the blueprints for life in its sequences of nucleotides. DNA is a molecule that consists of two strands of polynucleotide chains, see Figure 3.1. These very long chains (or strands) consist in turn of four types of nucleotide subunits. These subunits consist of a sugar (deoxyribose) attached to a phosphate and a nitrogen-containing base, which may be either adenine (A), thymine (T), cytosine (C), and guanine (G). Since it is the nitrogen-containing bases that differ in the nucleotide subunits, the symbols A, C, G and T are commonly used to denote the entire nucleotide subunit.

The nucleotide subunits link together to form a strand of DNA in a linear fashion by simply attaching the 3' hydroxyl of one subunit to the 5' phosphate of another, see Figure 3.1. The resulting DNA strand has an inherent polarity due to the manner in which the nucleotides are linked, and may be used to identify the strand's two ends which are thus denoted the 3' end and the 5' end.

DNA consists of two polynucleotide strands that are held together by hydrogen bonds between the individual nucleotide bases on the two strands. This leads to a structure with nucleotide bases in the center and sugar-phosphate backbones situated externally. Strands of DNA will not bond at random due to the pairing rules of the nucleotide bases, which enforce adenine (A) to pair with thymine (T) with/via two hydrogen bonds and cytosine (C) to couple with guanine (G) with/via three hydrogen bonds. These pairing rules, as well as the characteristic double helix configuration, contribute to an energetically favorable configuration of the DNA.









3.2. PCR 23

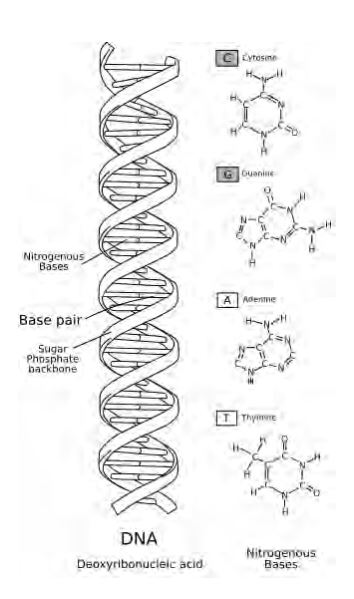


FIGURE 3.1. DNA is made of four nucleotide building blocks.

3.2. PCR

DNA has become the fundamental backbone of biological thought and as such an essential commodity for academic and industrial efforts to understand life and use this knowledge to help mankind. As such, DNA is naturally a necessary ingredient in an number of biotechnical analyses, making the accurate replication of specific DNA sequences an important process.

The fact that each strand of the DNA double helix is a sequence of nucleotide bases that complement one another according to the base pairing rules implies that each strand of the double helix can be used as a template for the synthesis of an exact copy of the entire DNA double strand. As can be seen in Figure 3.2, if it is possible to separate a length of DNA into two single strands, S' and S, the S strand will serve as a template for the building of a new S' strand and vice versa. This elegant replication process, together with an intricate control organization, ensures the rapid and accurate copying of vast amounts of genetic information. The actual amount of information that is copied is difficult to comprehend. In approximately eight hours, a dividing animal cell will copy nucleotide sequences whose combined lengths correspond to 10 000 theses like this one, while allowing on average only one or two erroneous letters.

The separation of the normally stable double helix configuration of DNA is performed by initiator proteins that break down the weak hydrogen bonds between the nucleotide bases. The position of this initial opening is called the replication origin, and is marked by a particular sequence of nucleotides that span around 100 base pairs. At this point, a group of proteins, a protein









3. POLYMERASE CHAIN REACTION

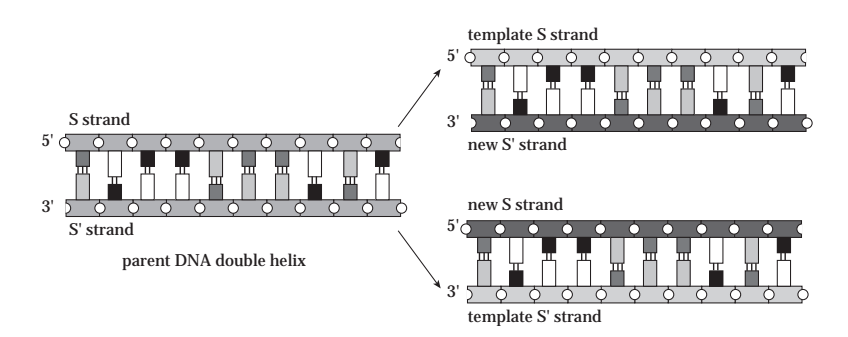


FIGURE 3.2. The two halves of the DNA double-strand will act as its on template for duplication.

machine, are utilized for the actual DNA replication. Protein machines travel along both ends of the initiated region, or replication forks, unzipping the DNA and copying bidirectionally.

The feat of imitating nature for the sake of copying DNA was achieved by Kary Mullis in the early 1980s, when he introduced the Polymerase Chain Reaction (PCR), see Saiki et al. (1985, 1988)), a feat for which he was endowed with the 1993 Nobel Prize in Chemistry. The introduction of PCR was a landmark event for biochemical analysis of DNA, since it allowed for the exponential amplification of specific DNA sequences in vitro. The replication process is naturally modelled on that which is used in the cell, but broken down into a discrete number of stages that are cycled over and over to achieve exponential DNA amplification, see Figure 3.3.

Instead of in the cell, industrial DNA replication is performed in a polypropylene reaction tube, see the inset in Figure 3.3. In this tube, the necessary ingredients for DNA replication are assembled in a reaction mixture, consisting of

- \cdot A double-stranded DNA molecule, the template which contains the sequence to be amplified.
- \cdot Two primers, one for each strand to be amplified, comprising of two single-stranded short DNA-oligos roughly 20 bases long.
- · dNTPs, a mixture of equal amounts of dATP, dTTP, dGTP, and dCTP, which are the nucleotide sub-units which will be put together to form new DNA molecules in the PCR amplification procedure.
- · DNA polymerase, preferable thermostable due to the high temperatures involved in the PCR-process. This is the enzyme which synthesizes the new DNA using the dNTPs.
- · Buffer, a solution that ensures optimal pH conditions for the PCR-process to take place. It also contains the necessary co-factor (i.e. Mg²⁺) for the polymerase to work properly.

The source DNA constitutes the specified DNA sequence which is to be copied. The amplification of the specified DNA sequences is achieved by using









3.2. PCR 25

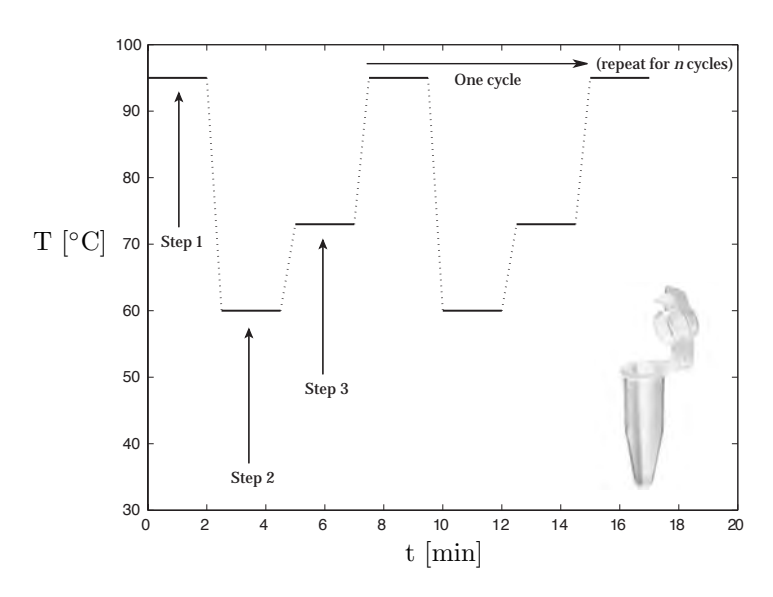


FIGURE 3.3. PCR temperature cycle indicating the three cycle stages, melting, annealing and synthesis. A standard PCR tube may be seen in the inset.

short, single-stranded DNA molecules called primers. Each primer is designed to bind to a specific region of the template with 100% match according to the base-pairing rules, one primer on the S-strand and the other on the S'-strand. The distance between the two primer-sites defines the stretch of DNA to be amplified, hence also the size of the final PCR-product. It is paramount to the success of the PCR that each primer only anneal to its designated stretch of DNA . The primers are short synthetic chains of specifically ordered bases, which are extended on single-stranded denatured DNA templates by a DNA polymerase, in the presence of deoxynucleoside triphosphates (dNTPs), and a buffer.

The stages that comprise the PCR cycle are 1) heat denaturation of the double-stranded DNA, 2) annealing of primers by cooling the mixture and 3) primer extension by DNA polymerase. Each repetition of the three-step protocol strand synthesis comprises an amplification cycle. Each new DNA strand synthesized becomes a template for a further cycle of amplification and the amplified DNA sequence is selectively amplified cycle after cycle. The three steps in the PCR amplification cycle, are described in greater detail below.

3.2.1. Denaturation

The first step in the PCR amplification system is the denaturation of the DNA sample which is achieved by raising the temperature to approximately 95°C, see Figure 3.3. During the denaturation, the double stranded DNA melts open to produce single stranded DNA, which is shown schematically in Figure 3.4.









26 3. POLYMERASE CHAIN REACTION

3.2.2. Renaturation or Annealing

For the second step of the PCR cycle, the temperature of the mixture is decreased to approximately 55° C, see Figure 3.3. A large excess of primers is used to favour primer-template formation instead of the competing (and non-productive) template renaturation that also occurs. The primers bounce around randomly due to Brownian motion. Hydrogen bonds are constantly formed and broken between the single stranded primer and the single stranded template. The more stable bonds (primers that fit exactly) last a little bit longer and on that little piece of double stranded DNA (template and primer), the Taq DNA polymerase can attach and start copying the template. Once a few bases have attached, the combined hydrogen bonds between the template and the primer is so strong, that it will not break.

3.2.3. Synthesis or Extension

In the third step, the temperature is raised to approximately 75°C, which is the ideal working temperature for the Taq DNA polymerase. The primers have a stronger attraction to the template, created by hydrogen bonds, than the forces breaking these attractions. Primers that are on positions with no exact match, loosen due to the increase in temperature and do not produce an extension of the fragment. The bases complementary to the template are coupled to the primer on the 3' side. The polymerase adds dNTPs from 5' to 3', reading the template from 3' to 5' side. Bases are added complementary to the template.

The PCR reaction involves numerous repeated cycles of DNA synthesis. Each cycle uses the products of the previous cycle as DNA templates, as is shown in Figure 3.4. In an industrial PCR process, a single DNA template molecule can produce millions of DNA products containing the sequence found between the two primers, after 30 - 40 cycles.

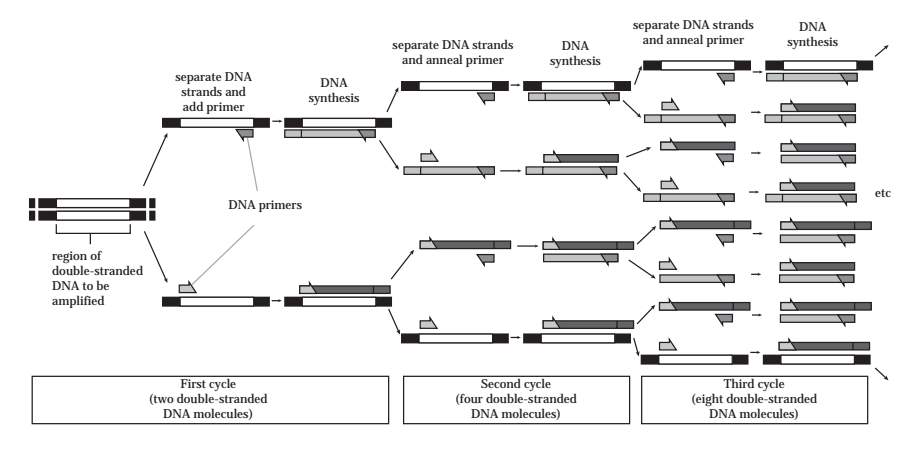


FIGURE 3.4. PCR amplifies a chosen DNA sequence in an exponential process.









3.3. IMPROVEMENTS

27

The success of an amplification process is gauged by monitoring the amount of replicated DNA by measuring the fluorescent intensity of a dye that is specific for the double stranded DNA in question. In Figure 3.5, amplification curves are presented for five dilutions (1:5, 1:10, 1:20, 1:40 and 1:80) and a negative sample of the HER-2 gene. A rapid and reproducible replication process resulting in high quality DNA product is achieved in this case.

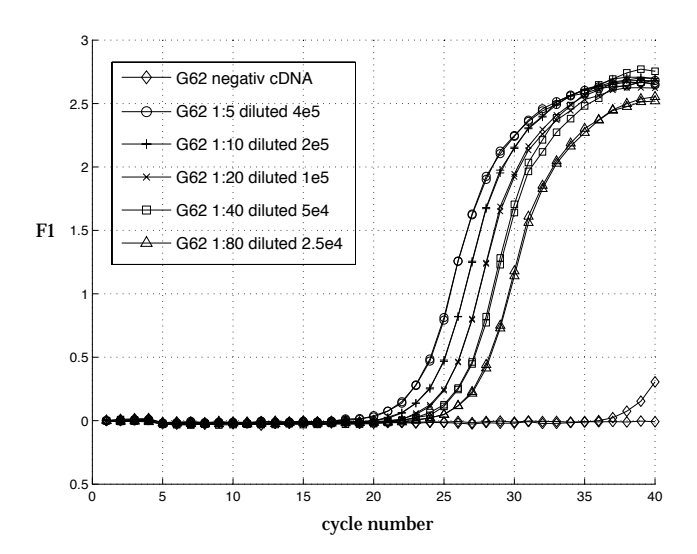


FIGURE 3.5. Fluorescent monitoring of rapid cycle PCR DNA amplification after compensating for the baseline signal. The target was a 120-bp region of the HER-2 gene. Samples were cDNA prepared from human breast tumour total RNA. Initial product concentrations from $2.5 \cdot 10^4$ copies up to $4.0 \cdot 10^5$ of G6PDH-2 and cDNA are presented. Two negative samples of cDNA were also included.

3.3. Improvements

A successful PCR process depends on a variety of factors, including the quality of the template, the choice of enzyme and primer design, as well as the amplification conditions used. However, the choice of the primer annealing temperature and the concentration of the magnesium ion in the reaction buffer are probably the most critical factors in designing a PCR of high specificity. These factors may require experimental optimization. Product contamination by undesired DNA sequences are problematic and should be avoided if possible for a successful PCR.

The time needed for each amplification cycle is also of great practical importance. In order to minimize this time period, one must attempt to optimize









28 3. POLYMERASE CHAIN REACTION

the conditions available at each of these steps described above, as well as minimize the transfer time between these steps. An important question that arises is how one may maximize cooling/heating rates, while also achieving optimal mixing quantities.

The temperature cycling procedure has historically been performed with Peltier elements, or variants thereof. Much effort has been spent in attempts to accelerate the amplification rate while ensuring a product of high quality. The most commonly applied strategy to obtain rapid temperature ramping has been to reduce reaction volumes combined with designing reaction vessels like capillaries (Wittwer et al. (1989)), cuvettes (Columbus et al. (1990); Petersen et al. (1991)), pipette tips (parallabs), ultra-thin-walled microplates (Hermann et al. (2004)) and various kinds of microfluidic devices.

A novel technique to enhance temperature homogenization utilizing a rotating sample disc was introduced by Malmquist (2004), see Figure 3.6. The initial hypothesis concerning this technique was that the flow of air over the exposed cones could be used as an effective temperature regulatory scheme for the PCR process. The prototype device that was developed proved to be both rapid and highly effective. In order to further probe the physical processes behind the technique, which combines buoyancy and rotational effects on a small volume of fluid, a collaborative study was initiated between Alphahelix Molecular Diagnostics AB and the Department of Mechanics. In the following, a brief overview of the theory behind this study is presented, as well as some illustrative results.



FIGURE 3.6. The tube is mounted horizontally on the 48-sample disc and rotated parallel to the symmetry axis of the disc. A white rectangle is inserted to illustrate the position of a PCR tube.









3.4. THEORY

29

3.4. Theory

The liquids used for a PCR analysis typically contain relatively low concentrations of template DNA. The material properties can therefore be reasonably well described by the Newtonian fluid model, where viscosity is taken to be a constant. Since the pieces of DNA being duplicated are small, the effects on the viscosity (compared with water) are negligible or small.

The basic equations of motion, for such a liquid, are the Navier-Stokes (N-S) equations. The N-S equations for flow of a Newtonian liquid in a rotating frame of reference may, in the Boussinesq approximation, be written as

$$\frac{\partial \vec{u}}{\partial t} + (\vec{u} \cdot \nabla)\vec{u} + 2\vec{\Omega} \times \vec{u} - \Omega^2 \vec{R} = -\frac{1}{\rho} \nabla p - \vec{g}_{\text{eff}} \beta (T - T_{\text{ref}}) + \nu \nabla^2 \vec{u}$$
 (3.1)

$$\nabla \cdot \vec{u} = 0 \qquad (3.2)$$

where ρ is the density of the fluid (which here will be close to that of water) \vec{u} is the velocity vector (in the rotating system), t denotes time, $\vec{\Omega} = \Omega \vec{e}_z$ is the system rotation vector, $\vec{R} = x\vec{e}_x + y\vec{e}_y$ is the vector perpendicular to the axis of rotation, that stretches from that axis to the fluid element, p is the pressure, and ν is the kinematic viscosity of the fluid. On the right-hand side of equation 3.2, in order to capture the buoyancy effects inherent in the system, i.e. the forces acting on the fluid due to variation in the density, the density is described as a function of the temperature in the centrifugal 'force' term using the Boussinesq approximation. T is the temperature ($T_{\rm ref}$ is the temperature at which the density is ρ), β is the volumetric expansion coefficient and $\vec{g}_{\rm eff}$ is the effective acceleration due to rotation, which in our case is $\vec{g}_{\rm eff} = \Omega^2 \vec{R}$. The gravitational acceleration ($-g\vec{e}_z$) is much smaller than the centrifugal 'force' ($\Omega^2 \vec{R}$) and can therefore be neglected.

The temperature field is coupled to the velocity field through the energy equation, which describes the evolution of the temperature distribution,

$$\frac{\partial T}{\partial t} + (\vec{u} \cdot \nabla)T = \alpha \nabla^2 T \quad , \tag{3.3}$$

where α is the thermal diffusivity.

For simplicity, the flow is described in a rotating frame of reference and two acceleration terms arise as a consequence in the momentum equation: the centrifugal 'force' $(\Omega^2 \vec{R})$ and the Coriolis 'force' $(2\vec{\Omega} \times \vec{u})$. The former is responsible for setting up a hydrostatic pressure gradient in the fluid and is not important for the dynamics. A reduced pressure $p^* = p - \frac{\rho}{2}R^2\Omega^2$ may be introduced, in order to rewrite the equations in a clearer manner. The Coriolis force is responsible for turning the flow towards the azimuthal direction. An effect of this force in nature is e.g. the curving of the trade winds due to the rotation of the earth.

The rotation rates used in the PCR method proposed by Malmquist (2004) are very high, of the order of 10^4 rpm. It is thus reasonable to believe that the Coriolis term will be instrumental in determining the qualitative features









30 3. POLYMERASE CHAIN REACTION

of the flow in a PCR tube. In the rotating system, the centripetal acceleration will be much larger than the acceleration tied to gravity. Thus, in that system, the centrifugal acceleration can be seen as an effective gravity $\vec{g}_{\rm eff} = \Omega^2 R \vec{e}_x$. In the NS-equations, it is obvious that the main balance will be between the Coriolis and buoyancy terms. This balance yields an estimate of the magnitude of the azimuthal velocity in the boundary layer that may be expressed as

$$u \sim \Omega R \beta \Delta T$$
 (3.4)

where $\Delta T = T - T_{\rm ref}$. Hence, the magnitude of the velocity is expected to scale linearly with both the rate of rotation Ω and the driving temperature difference ΔT

The Rossby number (Ro), which is the ratio between inertial and rotational (Coriolis) forces, may also be used to obtain an understanding of the rotational influence on the flow. Using the approximations above, the Rossby number may be expressed as

$$Ro = \frac{v}{\Omega L} \sim \frac{R}{L} \beta \Delta T \quad , \tag{3.5}$$

where L is the length of the tube. From expression 3.5, we conclude that Ro is independent of the rotation rate (Ω) . Thus, even though Ro is small, it will not tend to zero as the rotation increases. The consequence of this independence is that no radical changes in the character of the flow field will evolve due to an increase in rotation. This statement is true at least up to the limit where the flow becomes turbulent.

At rotational speeds around 10^4 rpm and a distance from the axis of rotation of 100 mm, the flow in a tube with L=7 mm will be laminar. We can judge this from the magnitude of the Grashof number, which expresses a ratio of buoyancy to viscous terms and is defined as

$$Gr = \frac{g\beta\Delta TL^3}{\nu^2},\tag{3.6}$$

with g replaced by $g_{\rm eff} = \Omega^2 R$. For turbulence to occur, the Grashof number should be larger than $10^9 - 10^{10}$. At 10^4 rpm, we can estimate Gr to be about 2×10^8 (for $\Delta T = 75^{\circ}$ C).

3.5. Hypothetical flows

Using the theoretical background presented above of this buoyancy and rotationally driven flow, a picture of a plausible flow field starts to emerge. The flow that evolves in the idealized PCR cone during heating is complicated. The main feature is the flow upward from the apex, which is highly unstable and generates rapid fluctuations, which enhance the mixing and rapidly give a uniform temperature.

In the absence of rotation, the heating would be less effective, since it is the strong force field created by the rotation that makes the buoyancy effects so









3.6. CALCULATIONS

31

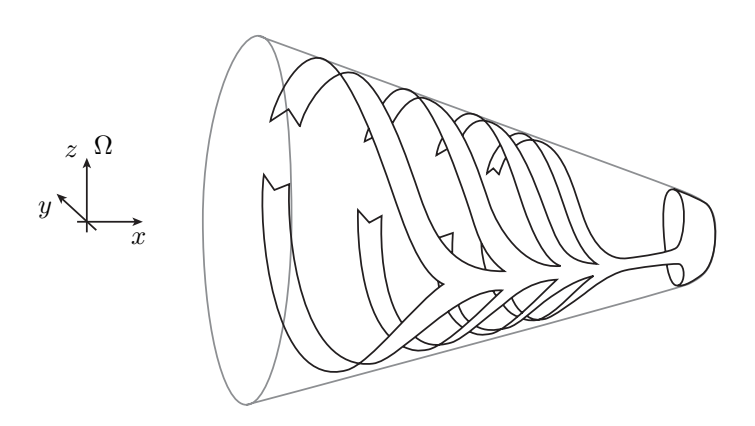


FIGURE 3.7. Schematic of the hypothesized boundary layer flow in the cone, in the case of a cone filled with warm fluid being rotated in a reservoir of cool fluid. The cooled fluid flows along the surface and masses at the tip of the cone.

powerful. With this said, we leave the case of heating and focus on the cooling process, which inherently poses some difficulties regarding the homogenization.

If we consider the non-rotating case with the acceleration of gravity directed towards the apex of the cone, and an ambient reservoir temperature lower than the fluid, the cooled fluid elements would be driven outwards along the whole inside of the cone towards the apex, resulting in a symmetrical toroidal flow in the cone.

This is in sharp contrast to the rapidly rotating case, where the main flow in the boundary layer is driven circumferentially along the wall in the azimuthal direction towards the mid-plane. If we look towards the apex and the rotation vector is directed upwards in the z-direction, the flow in the boundary layer will be from left to right in both the lower and upper parts. At the point where these flows meet, a stream is set up that will transport the cooled fluid towards the apex of the cone (the "effective" bottom of the cone). This flow is indicated in the schematic sketch in Figure 3.7. Thus, the flow inside the cone results in an accumulation of cooled fluid at the apex.

3.6. Calculations

To test the flow field hypothesis for the case of flow in a cone filled with warm fluid being rotated in a reservoir of cool fluid numerical simulations were performed with the commercial software package CFX. A somewhat simplified cone consisting of a truncated cone of length of 7 mm, base radius of 0.0025 m at x=0.1 m and apex radius of 0.0005 m at x=0.107 m was used. The volume of the cone is 50 μ L, which is a typical fluid volume in a practical PCR amplification device, where volumes from 20 to 100 μ L are common.





"gunderhaegg" — 2006/4/27 — 14:21 — page 32 — #39





32 3. POLYMERASE CHAIN REACTION

Heat transfer is allowed everywhere on the cone except at the base surface, where an insulated surface has been implemented. The calculations are initiated with a body of fluid that has a uniform temperature of 90°C and is at rest in the rotating reference system.

The results presented below are for a flow case where $\Omega=1000$ rpm and $\Delta T=75^{\circ}\mathrm{C}$. From these we may examine the main flow features proposed in the hypothesized flow. The flow and temperature fields are dynamically entwined and develop simultaneously in time. From the calculated temperature and velocity fields, two distinct phases in the development of the flow field are distinguishable. The first phase consists of a transient growth of the velocity in which the flow also changes directions. When the transient behaviour, after approximately half a second, has set up a stable flow field, the second phase begins in which the velocity slowly decreases, starting from the apex. This behaviour is closely related to a development of a stratified temperature field.

The difference in the temperature of the ambient air and the warm fluid triggers the flow. The fluid close to the wall is cooled and initially driven towards the apex due to the equivalent acceleration of gravity in that direction induced by the rotation. In Figure 3.8 a), the flow is shown in a xy-plane at the position z=0. The red colour at the walls represents the 'downward' flow in the x-direction towards the apex. This transient flow field is sustained only for a short period of time.

After about half a second, a quasi-stationary flow field is established where the downward flow, from being equally distributed in the cone, is concentrated to one side of the cone, see Figure 3.8 b). The reason for this behaviour is the Coriolis force. The flow towards the apex along the wall in Figure 3.8 a) is forced to turn into a flow in the azimuthal direction due to the Coriolis force producing a break in symmetry around the x-direction, see Figure 3.9. The two azimuthal boundary layers are flowing in the same direction and meet in a region where the flow turns towards the apex of the cone. The description above is expressed graphically in the schematic sketch in Figure 3.7. On the other side of the cone, the downward flow is weakened and eventually changes direction.

The axial flow at t=0.5 seconds is approximately four times larger than at t=0.1 seconds. The developed flow pattern shown in Figure 3.8 b) and 3.9 is then fairly constant until the velocities start to decrease. The decrease in velocities occurs initially at the apex. The reason for the decrease in flow velocity is that the temperature difference, which drives the flow, diminishes at the apex first, and develops into a stabilizing stratification. In the rotational case, a slow flow back (to the left in Figure 3.9) through the core is also visible. This back flow forms two vortices together with the boundary layers.

From the previous chapters in the introduction, it is easily understood that the Coriolis force creates a flow which is completely different from that of a non-rotating case. In the case of a non-rotating cone, the downward flow would be equally large around the wall with the upward flow concentrated in the middle of the cone in an axisymmetric toroidal pattern. The azimuthal flow would be









3.6. CALCULATIONS

33

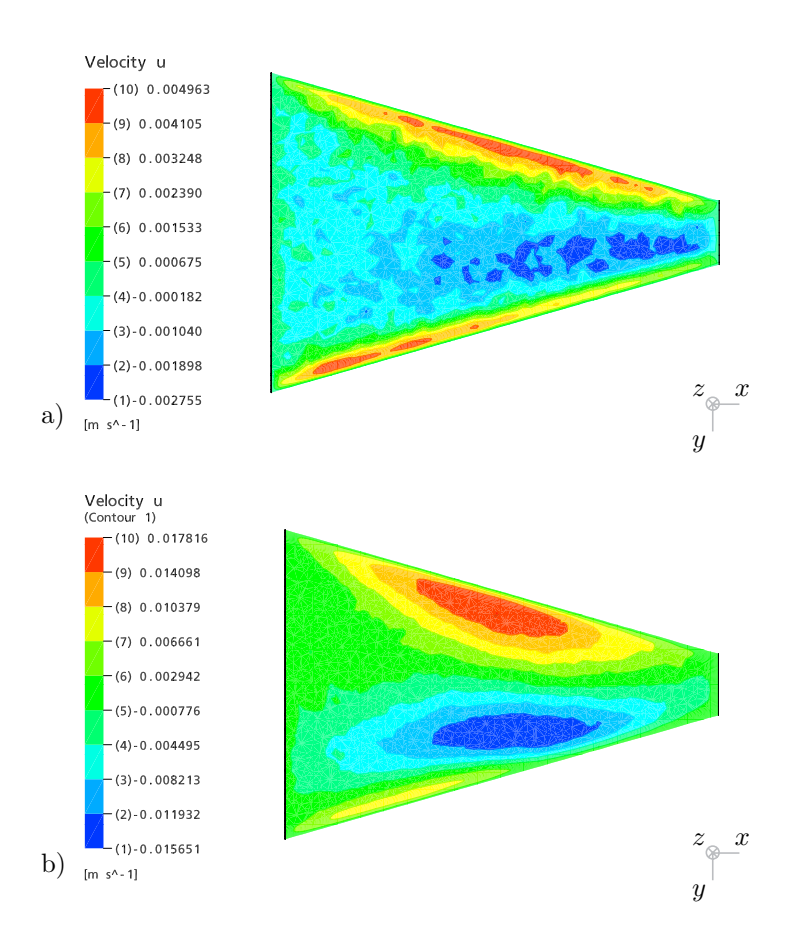


FIGURE 3.8. The flow field in the horizontal plane at z=0 after a) 0.1 seconds and b) 0.5 seconds of cooling. The view is from below and the rotation clockwise around the z-axis. Red colour denotes flow towards the apex. Blue colour denotes flow towards the base.

zero in this case. The introduction of rotation introduces a symmetry break to the flow in the form of the Coriolis-driven flow in the azimuthal direction, which is analogous to the secondary flow in a rotating duct.









34 3. POLYMERASE CHAIN REACTION

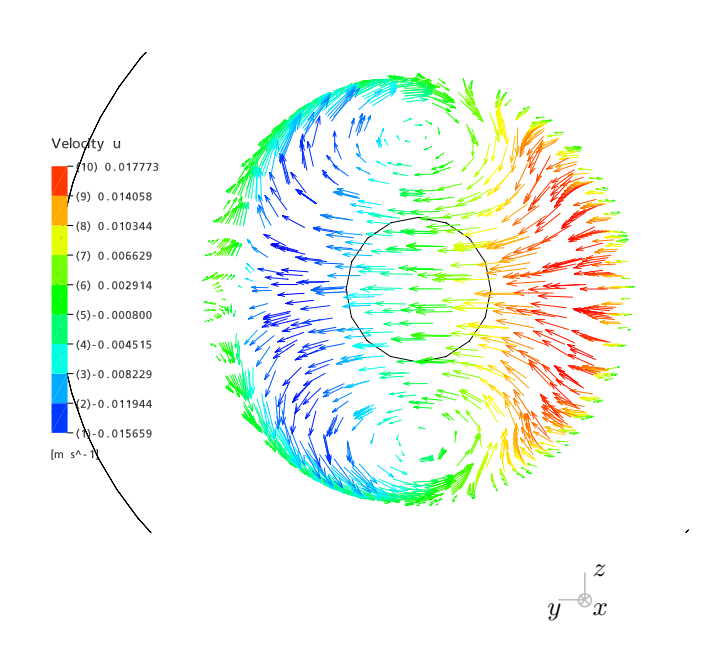


FIGURE 3.9. The same flow field as in Figure 3.8 b), shown in a cross-plane taken through the middle, looking towards the apex (the small black circle). Arrows: velocity in the plane, colours represent the velocity in the third direction (red colour denotes flow towards the apex).

For the DNA replication process, the primary variable is temperature. It is of great importance that the temperatures tied to the three steps of the PCR process (denaturation, annealing and extension) are reached quickly and accurately. In Figure 3.10 the development in time of the temperature at the base, middle and apex of the cone is presented. It is immediately evident that the temperature decrease is very rapid throughout the cone. The spread of temperatures in the cone is also large.

Also presented in Figure 3.10 are temperature curves for three different heat transfer coefficients, h = 500, h = 1500 and $h = \infty$. The introduction of a finite heat transfer coefficient results in a slower temperature decrease, while increasing the homogeneity of the temperature decrease over the cone.

Due to the collaboration with Alphahelix Molecular Diagnostics AB, experimental data for the flow configuration studied were available. This data included temperature measurements inside the PCR cone at specific positions along the x-axis. made with miniature gold-plated thermistors. The thermistors have a diameter of 0.37 mm and have an accuracy of $\pm 0.1^{\circ}$ C. The temperature was sampled throughout standard PCR-cycles. If these experiments are compared with the calculations several interesting observations may be made. Although the trends of the measurements and calculations are similar, there









3.7. SUMMARY

35

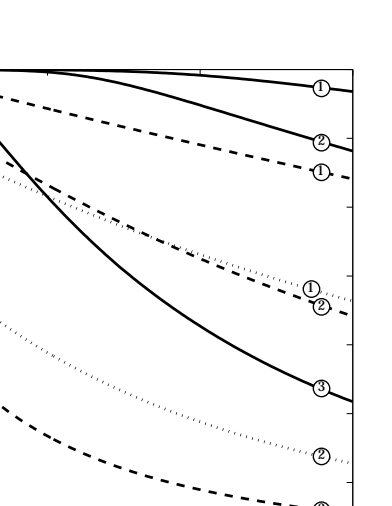


FIGURE 3.10. Temperature development as a function of time. Ω =1000 rpm. (1) h=500, (2) h=1500, (3) Fixed temperature. — base, — middle, · · · apex.

t [s]

seems to be an overestimation of the cooling rate and temperature spreading in the calculations. This may be due to the positioning of the probes in the PCR-cone, which due to the relative size of the probe is quite arduous. It may also be an artifact of the chosen heat transfer coefficient h, indicating that this value should perhaps be somewhat smaller than 500.

Further details concerning the numerical calculations and practical implications of these theories are available in Papers 5 and 6.

3.7. Summary

80

70

60

50

40

30

20

10L

0.5

T [°C]

This study was initiated in order to gain a better understanding of a flow constructed to produce a more rapid and effective process for the amplification of DNA sequences using PCR. While the system was constructed to produce an effective method of temperature control due to the flow of air over a cone, a much more complex (and interesting) flow was hidden inside the cone. A superposition of buoyancy and rotational effects resulted in an internal flow that not only increased temperature homogenization, but also increased the mixing of the PCR mixture which perhaps in itself will increase the effectiveness of the annealing and extension processes once the temperature plateaux are reached.









CHAPTER 4

Blood flow in the brain

In the previous chapters, we have been exposed to applications of fluid mechanics ranging from the separation of creme from milk, turbine motors, microfluidic mixing and DNA replication. In all of these cases, rotational effects have been important for the fluid motions being examined. In this chapter, we will delve into another exciting and important area of fluid dynamic research, where rotational effects may be viewed, not as the most important effect on the flow, but instead as one of many layers of complexity. This area is hemodynamics.

4.1. Introduction

In the spring of 2004, the Department of Mechanics, KTH, the Department of Neuroradiology, Karolinska University Hospital and Philips Medical Systems initiated a collaboration to probe the potential of conventional x-ray in obtaining quantitative information about brain blood flow characteristics. Of particular interest was flow in connection to malformations of blood vessels in the brain, specifically aneurysms and arteriovenous malformations, with the long term aim to create better predictive models for risk for intracranial hemorrhage and treatment effects, in order to optimize individual management.

The study of hemodynamics (Greek haimo: blood, dynamis: power) is truly a layer cake of complexity. In the place of the flow of a Newtonian fluid in rectangular ducts with smooth, rigid walls, we are faced with a system with irregular tortuous geometries, flexible walls and in addition pulsatile (sometimes turbulent) flow of a non-Newtonian fluid. Where should we start? Simplifications are certainly necessary, but before these are presented, let us see what kinds of systems the blood that we wish to study is flowing through. For sundry reasons, we have limited our studies to the arterial system for the time being.

4.2. What can go wrong?

In Western Europe, approximately two percent of the total population will at some time be affected by a cerebral arterial aneurysm. Brain arteriovenous malformations (AVM) are ten times less common, but stand behind arterial aneurysms as the second most common cause of spontaneous intracranial hemorrhage in the population <40 yo. In the European Union alone, with its present population of approximately 375 million, over 8 million people will over the course of their lifetime harbour a cerebral aneurysm or brain arteriovenous malformation that if diagnosed should in a large number of cases be









4.2. WHAT CAN GO WRONG?

37

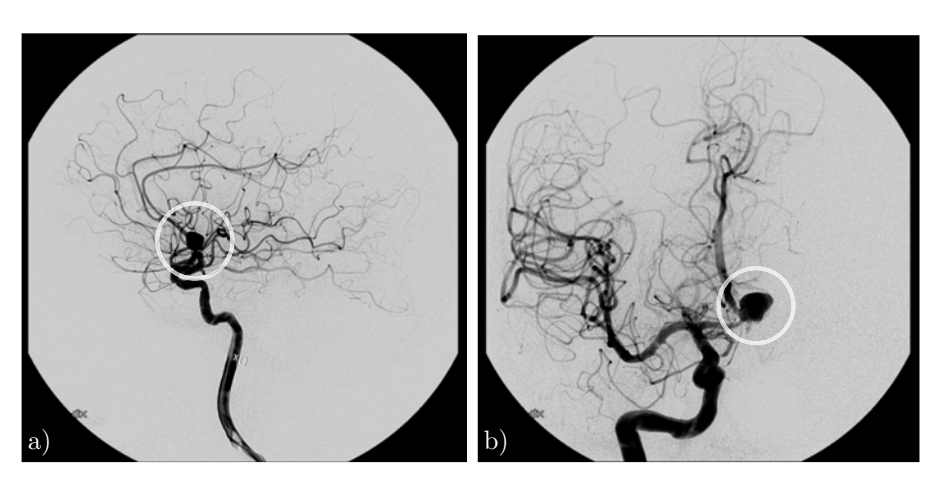


FIGURE 4.1. Cerebral angiography. Subtracted images, showing only contrast medium. 59-year-old male patient who presented with intracranial hemorrhage. The aneurysm is the rounded structure encircled in white in a a) frontal and b) lateral view (from the side).

amenable to treatment. Today we have very limited knowledge about which factors cause an aneurysm or a brain arteriovenous malformation to rupture, the most feared event. Hemodynamic stress is probably very important since it weakens the vessel wall and subject it to focal tension which induces angiopathy (Pile-Spellman et al. (1986)).

4.2.1. Aneurysms

An aneurysm is a localized dilation or ballooning of a blood vessel. Aneurysms most commonly occur in the arteries at the base of the brain, specifically in the *Circulus Willisii*. Aneurysms are also prevalent in the aorta. The formation of intracranial aneurysms is likely to be influenced by genetic, structural, metabolic and hemodynamic factors. The hemodynamic processes are not necessarily limited to the macroscopic scale, such that a powerful pulsatile flow could cause an aneurysm to rupture. At the microscopic level, it has been found that an oscillatory, but not a steady, stress is successful in activating inflammatory processes in endothelial cells, see Sorescu et al. (2003). X-ray images of an intracranial aneurysm are shown in Figure 4.1.

4.2.2. Arteriovenous malformations

On its way to provide the brain with nutrients and oxygen, blood should enter at high pressure and velocity through the major cerebral arteries, continue through smaller and smaller arteries and arterioles until the capillary bed is reached. Blood moves through the capillaries, giving up oxygen and taking up waste products from the surrounding cells. Capillaries successively join together, one upon the other, to form the venulae and veins that carry blood









38 4. BLOOD FLOW IN THE BRAIN

back to the heart and lungs at a relatively low pressure and at lower speeds. It is then replenished with oxygen and the whole process is repeated.

If an arteriovenous malformation (AVM) is present in the brain, as is the case for the patient imaged in Figure 4.2, the descent to the capillary bed is replaced with a tangle of interconnected vessels of various sizes, but all larger than a capillary vessel. This tangle of blood vessels, called a nidus forms a relatively direct connection, or shunt, between high pressure arteries and low pressure veins.

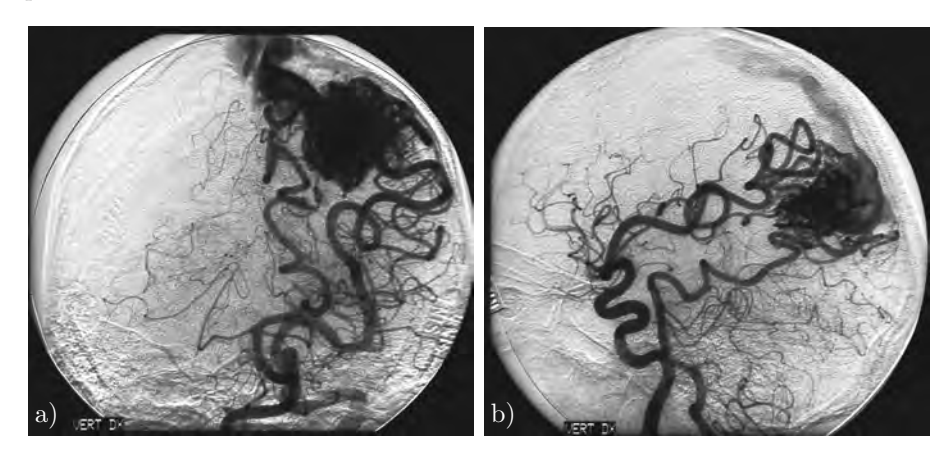


FIGURE 4.2. Cerebral angiography. Brain arteriovenous malformation in a 50-year-old male patient. a) the frontal and b) lateral view.

There are multiple risks combined with the presence of AVMs in the brain. The abnormal assemblage of vessels does not perform the necessary exchange of nutrients and waste materials, vital for the normal function of the brain. The vessels in the nidus are abnormal in that they lack the smooth muscle layer present in normal arteries, making them fragile and prone to bleed. The high flow and elevated pressure in vessels as the blood enters the venous network may also contribute to hemorrhages or seizures.

4.3. How do we notice this?

A doctor once stated that, "The goal of our treatment is not to cure the patients, but to keep them free from symptoms of the disease, until they die from something else." A very wide range of symptoms prompt people with intracranial hemorrhage to seek health care. For example, seizures, persistent or severe headaches, double vision, or loss of motor or sensory functions in limbs, coma or sudden death can all be related to aneurysm or AVM rupture or local mass effect on surrounding brain tissue.

A majority of brain hemorrhages are minor and are stopped by the body's own processes of hemostasis. The damage varies according the location and volume of the hemorrhage. Major hemorrhages are life threatening and if









39

4.4. HOW DO WE VISUALIZE THE BLOOD VESSELS?

hemostasis does not occur the patient dies. Other potential problems are for example that blood in the subarachnoid space, a space in between the skull and the brain, may block the circulation of cerebrospinal fluid (CSF), causing a build-up of fluid in the subarachnoid space and with this an increased pressure on the brain. The increase in pressure may cause the open spaces in the brain (ventricles) to enlarge, causing the state known as hydrocephalus. Symptoms connected with hydrocephalus are lethargy, confusion and incontinence.

The blood that escapes from a ruptured vessel into the subarachnoid space around the base of the brain can also produce a problem called vasospasm. Vasospasm typically develops 5-8 days after the initial hemorrhage and is an uncontrollable contraction of the arteries, which may lead to brain ischemia, general of focal. A severe constriction of a brain vessel due to vasospasm can impede the flow of blood to such a degree that a stroke and even death may result. Vasospasm may be alleviated with pressure elevation, blood dilution or medical therapy aimed at the vessel wall. Local balloon dilatation of the vessels may be used in severe cases.

Thus our aim is to alleviate the symptoms and to prevent further events such as a future hemorrhage, which will again be symptomatic.

4.4. How do we visualize the blood vessels?

The clinical visualization tools, i.e. angiography or x-ray examination of vessels, such as those shown in Figures 4.1 and 4.2, have evolved tremendously since the first steps were taken by Reyner and Glover (1897) who pioneered the method of injecting x-ray contrast media to obtain information about vessel morphologies. This technique was adapted for cerebral examinations by Moniz (1927) and continuous technological advances have carried the technique into the 21st century.

Abundant computing power has enabled the use of standard x-ray sources for new imaging techniques, such as computerised tomography (CT), introduced by Hounsfield and Cormack (Cormack (1963)), digital subtraction angiography and 3D rotational angiography. The introduction of magnetic resonance imaging, which utilizes the relaxation properties of excited hydrogen nuclei in water in the body, is revolutionizing the science of physiological imaging, and data from the two modalities may be merged.

4.4.1. Cerebral angiography

This study focuses on the use of conventional x-ray angiography to obtain quantitative quantitative cerebral blood flow information. Cerebral angiography involves the passing of a catheter into a large artery, most often the femoral artery in the groin, and advancing this catheter via the aorta through the carotid artery up to or into the brain. With the catheter in place, a radiopaque contrast agent is injected and a series of radiographs is taken while the fluid travels through the vasculature. The beginning of the series thus shows the arterial vasculature and it can be continued in order to capture the venous circulation.









40 4. BLOOD FLOW IN THE BRAIN

4.5. What can be done?

The choice of treatment for a patient with an aneurysm or AVM must take into account both the protective effects as well as the possible risks tied to a given procedure. To not treat a patient is occasionally a viable alternative.

While the surgical removal or isolation of an aneurysm or AVM is an effective curative treatment, an increasing number of patients are being treated through interventional neuroradiology, i.e. via the blood vessels rather than through open skull surgery. The method is, very briefly, to introduce a flow controlling device into the diseased vessel.

4.5.1. Guglielmi Detachable Coil (GDC)

One of the most common devices used in the treatment of aneurysms is the Guglielmi Detachable Coil (GDC). The coils consist of platinum wire with a diameter of approximately 0.25 mm, delivered in different lengths and diameters. The coils adapts to the shape of an aneurysm and can be used to fill the lumen, much like a ball of yarn. Coils can be used either to block blood flow to the affected area or to fill the aneurysm or fistula, thus preventing a rupture. In Figure 4.3, pre- and post-treatment images of a cerebral aneurysm are shown. Studies have shown that when endovascular coiling and neurosurgical clipping are both therapeutic options, the short-term risks of complications are lower with coiling (Molyneux et al. (2002)). Today there are many manufacturers of coils, but all have the same functionality.

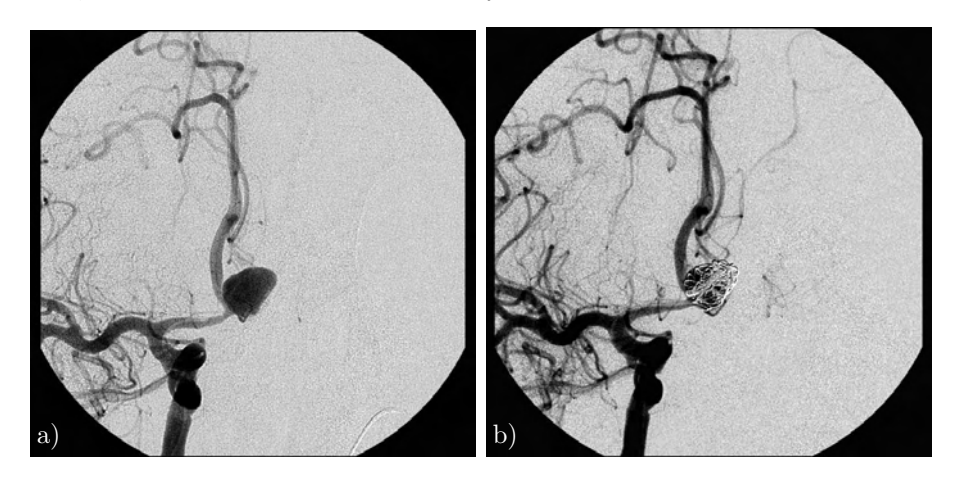


FIGURE 4.3. Cerebral angiography, frontal view. Aneurysm in a 59-year-old male a) before and b) after partial treatment with a Guglielmi Detachable Coil.

4.5.2. Glue

In more morphologically complex malformations, such as AVMs, a glue-like substance may be injected through a microcatheter to embolize a single vessel









4.6. FLOW MEASUREMENTS

41

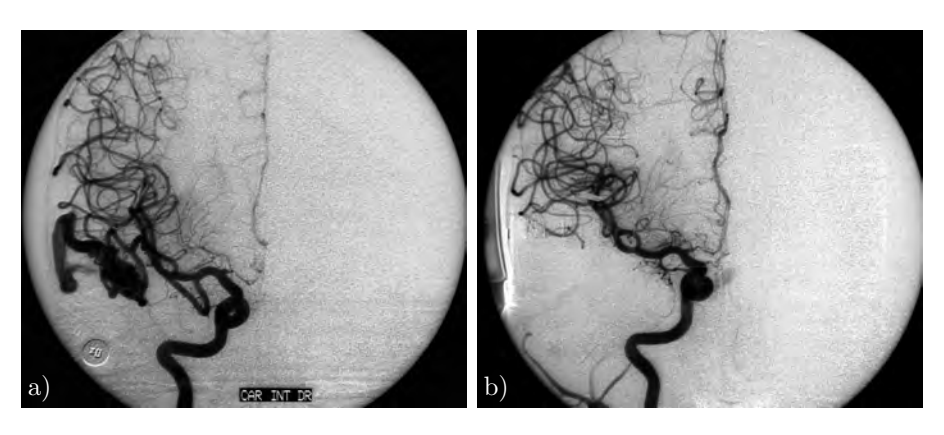


FIGURE 4.4. Cerebral angiography, frontal view. AVM in a 46-year-old-male a) before and b) after treatment with embolizing glue.

or group of vessels as it solidifies. The technique, introduced by Luessenhop and Spence (1960), is highly dependant on the flow conditions in the vessels that are to be occluded. In Figure 4.4, an AVM is shown before and after complete embolization with glue. The two major disadvantages with glue is that there must be good access through the vasculature and that the cure rate is low, in the best of hands around 40%.

4.5.3. Gamma Knife

AVMs may also be treated with radiation. The Swedish physician Lars Leksell pioneered the precise application of a controlled radiation dosage to the volume of the brain occupied by an AVM (Leksell (1951)), although the first treatment was reported by Steiner et al. (1972).

The radiation is administered using 201 Cobalt-60 sources that individually do not cause damage to the brain as the γ -rays pass through it. At the focal spot, which has a positioning accuracy of a fraction of a millimeter, the radiation from all the sources converge and the very high radiation dose damages the vessel wall and induces fibrosis and later thrombosis and obliteration. It takes tow to three years after the single treatment for the targeted vessels to occlude. The technique has been proven effective especially for small, deeply located AVMs. For large AVMs, there is a considerable risk for adverse radiation effects which limits the usefulness of the technique.

4.6. Flow measurements

Much is unclear concerning the genesis, growth and rupture of cerebral malformations. Therefore, additional quantitative information concerning the blood flow in malformations is desirable in an attempt to improve predictive models for the natural course of the disease, as well as in the process of treatment evaluation. It is known that some AVMs are radiation resistant , but the reason





"gunderhaegg" — 2006/4/27 — 14:21 — page 42 — #49





42 4. BLOOD FLOW IN THE BRAIN

is not clearly understood. It has been conjectured that the success of radiosurgery is inversely related to the flow rate in the AVM, but this hypothesis has not been tested in a prospective study.

In the case of aneurysms, hemodynamic effects have gained recognition concerning their role in their pathogenesis, as well as thrombosis, see Metcalfe (2003). Hemodynamic factors, such as wall shear stress pressure and jet impingement, are central in the reasoning of for example Cebral (2005) in novel treatment planning work flows.

The flow information may not only be useful as an indicator of future effects on the vessel of unchecked flow, but also as an immediate objective gauge of the effect of an intervention.

Information about a cerebral blood flow can be made available through a number of different techniques. Flow speed, as well as vessel morphology, for superficial cranial vessels can be measured using Doppler ultrasound (Walter et al. (1986)). Localized measurements in the body may be made using catheter mounted pressure and temperature probes Gabe et al. (1969). Three-dimensional flow fields can be acquired using phase contrast magnetic resonance imaging (PC-MRI), see Firmin et al. (1987); Walker et al. (1988). The inherent temporal and spatial resolution of MR techniques limit the viability of these techniques for fast flows and/or small vessels, but research in this area is abundant and will certainly lead to great leaps in quality for these kinds of measurements.

The possibility of using the dynamic acquisition of contrast injection using digital subtraction x-ray has also been probed by many investigators. Extracting mean flow quantities of blood flow utilizing localized time-intensity curves was studied by among others Schmiel et al. (1978) and Spiller et al. (1983). These methods yielded bulk flow results with an uncertainty of less than 10% for steady flows.

Stereoscopic digital subtraction angiography (DSA) brings morphological information to the flow measurements. This practice was extended by Schmitt et al. (2005) who used a rotational x-ray angiography to obtain the vessel structure. The two-dimensional dynamic flow information was then mapped on the three-dimensional structure via a forward-projection algorithm. The authors showed that the method is robust, but they did not perform well-controlled experiments to assess accuracy and reproducibility.

The goal of this study was to assess said accuracy and reproducibility. A series of phantom measurements were therefore performed to validate the software and methodology of Schmitt et al. (2005), as well as to judge the possibilities to implement it into a clinical environment. The final aim was to create a tool to assist in the choice of interventional procedure and materials, as well as to assess its impact on flow and shear stress.

4.7. Materials and Methods

The proposed methodology demands two sets of data in order to extract threedimensional flow quantities. The first is a three-dimensional representation of









4.7. MATERIALS AND METHODS

43

the vessel morphology. The second data set consists of a temporal registration of the injection of a contrast agent into the vessel of interest.

4.7.1. 3DRA

During a rotational scan, one hundred images are acquired as the C-arm of the x-ray equipment moves along a semicircular trajectory of 240 degrees. At the same time contrast media is injected through a catheter in a cervical artery. The image quality of the vessel reconstruction is highly dependent on the degree of contrast agent filling of the vessel. The choice of injection protocol has been shown to of great importance and will be discussed later in this report.



FIGURE 4.5. Motion of the C-arm during a rotational scan. The initial (1) and terminal (3) positions are shown together with one intermediary (2) position. A conical beam is emitted from the source and penetrates the object to be studied.

Data from the 100 projections during the C-arm rotatory movement are the basis for the three-dimensional reconstruction that is realized using a backprojection algorithm, see Feldkamp et al. (1984); Grass et al. (1999a,b). The result of this process is a matrix in three dimensions that represents the spatial distribution of X-ray attenuation of the tissue. Volumes with high attenuation, such as bone and contrast-filled vasculature, are represented with high values in the matrix.









44 4. BLOOD FLOW IN THE BRAIN

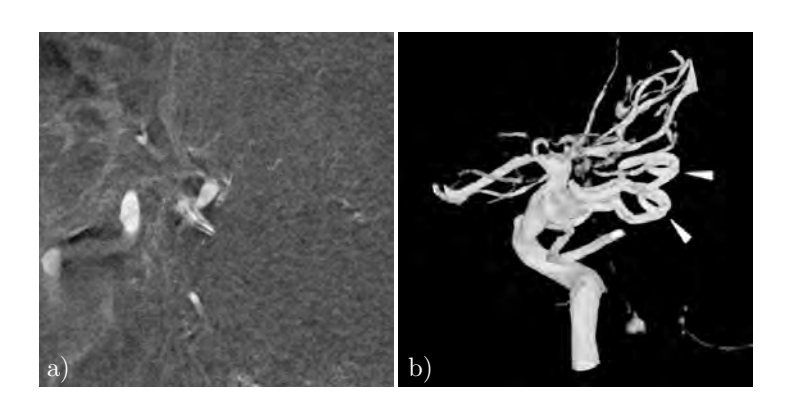


FIGURE 4.6. An example of a 3-dimensional volume (256^3 voxels) reconstructed from rotational angiography projections. A segment, i.e. a slice, of the intensity field is shown in a), while b) shows a reconstruction of the vasculature as well as the removal of unwanted information by thresholding. The arrowheads point at two metallic clips that are visible due to their high density.

4.7.2. 3D segmentation

The rotational scan does not immediately produce a three-dimensional morphology, but instead a three-dimensional matrix of intensity voxels. In order to extract a useable morphological volume, represented by a limited number of high intensity voxels, from the intensity space consisting of a large number of voxels, up to 512^3 , an effective vessel segmentation technique is necessary. The 3DRA software utilizes the Foot-Foot software developed at Philips Research Laboratories, see Bruijns (2001).

The Foot-Foot method analyses the distribution of intensities for the voxels of the 3DRA image matrix and establishes two thresholds for the data. These thresholds are then used to separate vessels from background tissue. Areas that have voxel values between these thresholds are classified as potential vessel voxels.

4.7.3. Region growing

The goal of this project was to be able to track a front of contrast agent through a vessel tree and thus calculate the flux of blood through the vessel at any given point. First it was necessary to define areas in which the contrast intensity could be evaluated. The segmented volume obtained using the Foot-Foot method results in a binary matrix where voxels are either part of the vessel (1) or outside the vessel (0). In order to introduce information concerning the internal positioning of the vessel voxels, a region growing algorithm was applied to the vessel matrix. This procedure grouped the vessel voxels in approximate cross-sectional slices of the vessel structure.









4.7. MATERIALS AND METHODS

45

The region-growing algorithm may be seen as a propagation of a voxel wave through the vessel. The procedure is initiated by defining a seed voxel, from which the voxel wave will emanate. For our purposes, the seed voxel is chosen as the most proximal voxel in the binary matrix volume. In the next step adjacent voxels are grouped into a voxel cluster that is assigned a cluster number. Consecutive clusters are obtained by the step-wise propagation of our voxel wave. In Figure 4.7, a two-dimensional example of the cluster growing algorithm is illustrated.

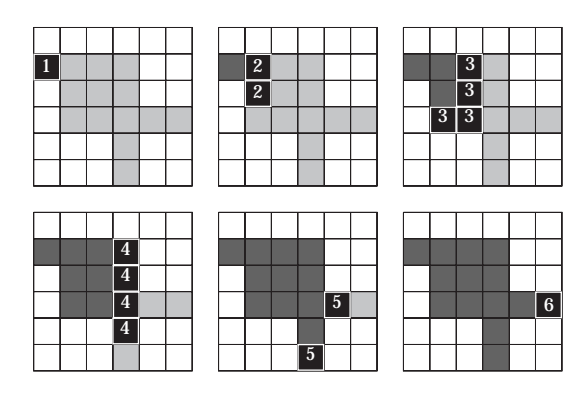


FIGURE 4.7. A two-dimensional example of the region growing algorithm used to create cross-sectional clusters of a vessel tree. The seed voxel is labeled 1 in the upper left-hand corner of the matrix. The consecutive clusters labeled 2 to 6 trace their way through the grey vessel voxels. Note the bifurcation that is detected in step 5. Reproduced with permission from Schmitt et al. (2002)

The region growing algorithm registers a bifurcation as the point where a wave becomes disjoint. The relative positions of the clusters are registered as the region growing procedure is carried out. The method was described in detail in Cornelia et al. (1995) and was modified for this project according to Schmitt (2000).

4.7.4. Flow

The second data set necessary for the procedure is a temporal collection of images of the injection of contrast agent into the vessel tree of interest. The temporal images are acquired at 50 Hz and at a spatial resolution of 512×512 pixels. The high flow speeds known to occur in cranial arteries and associated pathologies require a high temporal resolution. Standard injection protocols for the major arteries were used. The specific protocol will be indicated in each case that is reported.









46 4. BLOOD FLOW IN THE BRAIN

4.7.5. Forward projection

To track the propagation of contrast agent, the acquired two-dimensional flow information was mapped onto to the three-dimensional vessel. This was performed using a forward projection technique. This technique states that a ray that emanates from the source of the x-ray will intersect the vessel in the three-dimensional vessel matrix, as well as the two-dimensional flow detector pixel, see Figure 4.8. Positions for the source, detector plate and three-dimensional measurement area are all known from the system calibration procedure.

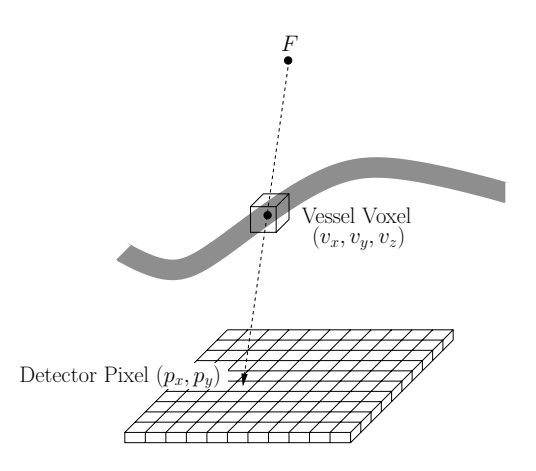


FIGURE 4.8. A schematic of the ray analogy used to relate the positions of the x-ray source (F_x, F_y, F_z) , 3DRA vessel position (v_x, v_y, v_z) and flow acquisition position (p_x, p_y, p_z) . Reproduced with permission from Schmitt (2000).

The intensity registered at a certain point in the flow acquisition is a function of contrast in a three-dimensional reality. The intensity value that is stored for a certain voxel is the average for all voxels in that cluster, and as such can only carry with it information concerning the flux of blood flow through the chosen cross-sectional cluster.

4.8. Experiments

In order to test the validity of the proposed algorithms, idealized flow situations where the true flow conditions were either known or could be calculated were necessary. Steady, laminar flow through a smooth-walled cylindrical pipe was the first flow studied. The pipe was encapsulated in a water-filled Plexiglas cylinder, see Figure 4.9. The water in the phantom attenuates the x-ray radiation in approximately the same way as brain tissue. The material of the phantom absorbs and scatters the incoming x-rays in a manner similar to the bone and tissue. Spiers (1943) showed that the model material should have





"gunderhaegg" — 2006/4/27 — 14:21 — page 47 — #54





4.9. RESULTS 47

the same density and contain the same number of electrons per gram as the material being modelled.

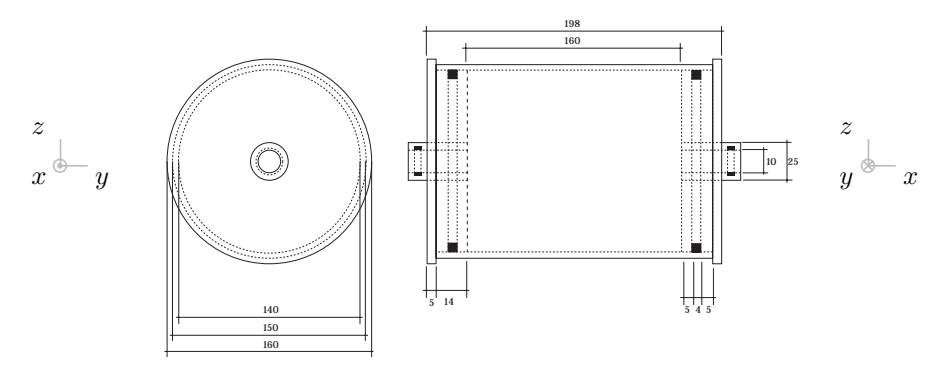


FIGURE 4.9. The validation flow pipes were encapsulated in a water-filled cylinder in order to model a proper human head. All measurements are in millimeters.

The injection of contrast agent was performed in accordance with the clinical work-flow used at the Department of Neuroradiology at KS, see Figure 4.10. All of the materials used, from the injection device, to the contrast agent and the catheters, were clinical stock.

The injection of contrast agent was performed through catheters. Two guiding catheters of differing inner diameters, 0.035 in (4F) and 0.056 in (5F), were utilized in the study. The system also implemented units of salt solution to flush the system before and after injections.

The injection protocols used to control the introduction of contrast agent into the flow were also chosen from those used in the clinical situations. For the rotational run, a 4 mL/second, 20 mL total volume, 2 second delay (hereafter called 4-20 injection) injection protocol was used. For the flow acquisitions two injection protocols were utilized, 6 mL/second, 9 mL total volume, and 4 mL/second, 9 mL total volume, both with 0 second delays. These injections are referred to as 6-9 and 4-9 injections.

4.9. Results

4.9.1. Phantom studies

The first flow case was steady laminar flow in a cylindrical pipe. The results below concern a series of experiments where flow acquisitions were made for three different flow speeds in a straight cylindrical pipe of diameter 6 mm, which is slightly larger than the human internal carotis artery (cervical vessel).

It is instructive to study a temporal contrast density data series. In Figure 4.11, the contrast density has been plotted a a function of time during steady laminar flow (Flow case A, see Paper 7) and after a bolus injection of contrast agent through a 4F guiding catheter. Curves are presented for a small number of the clusters produced by the region growing algorithms. The total









48 4. BLOOD FLOW IN THE BRAIN

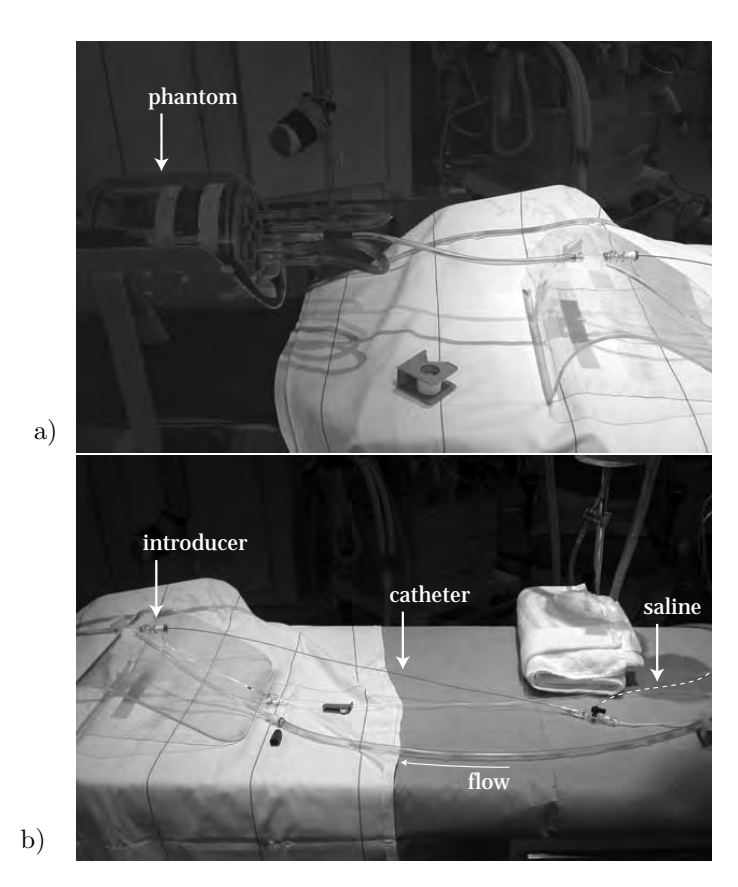


FIGURE 4.10. Photography of the experimental set-up. The injection of contrast agent is supplied through standard clinical connections. The flow is from right to left and the phantom is to the far left in a).

number of clusters was limited to 150, but was approximately 110 in the cases studied here.

The method used to calculate the velocity of the fluid flow in the pipe is based on the measurement of the propagation of the contrast front as it is registered in consecutive digital image frames. Instead of choosing a certain number of curves for the evaluation of the flow velocity, the entire experimental sampling is presented in a contour map from which the values are extracted.

It is clear from Figures 4.12a) that the choice of contrast intensity level affects the velocity level that is extracted from it. In each of these plots, a contour intensity level of 100 has been inserted to exemplify the behaviour of the injection of contrast agent in space and time. For these steady flows, the slope of the arrival of contrast agent is clearly linear. A least-square fitting of a straight line has been fitted to the data and superimposed in Figures 4.12









4.9. RESULTS 49

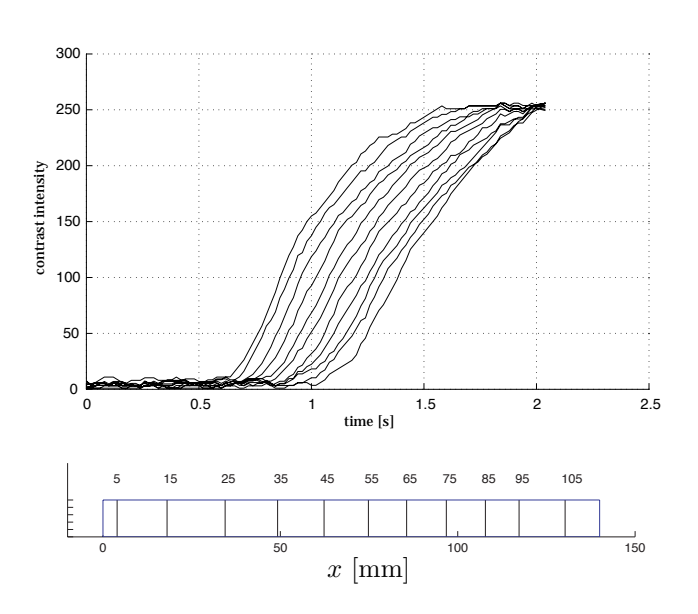


FIGURE 4.11. Time-intensity curves and clustering of the flow reconstruction for a 6-9 injection through a 4F catheter for flow A. The curves from left to right represent the consecutive clusters, with their respective numbers, presented in the localization figure under the contrast intensity plot.

a) and b). The slope of this linear fit is the speed of the propagation of the contrast intensity level through the tube.

The injection protocol used has a strong effect on the extracted velocity results. Forcing even a small volume of fluid through the minute catheters produce a violent jet that will both enhance mixing with the flow and increase the fluid flux. For clinically valid flow speeds, the injection speed is of the same order as the blood flow speed. For the 6-9 injection, the increased flow is approximately 5% of the total flow.

The mean flux Q through the tube is calculated via Q = VA, where V is the flow speed and $A = \pi r^2$ is the cross-sectional area of the tube. For a laminar flow profile $\frac{1}{2}u_{\max}A$, where u_{\max} is the maximum speed. If it is assumed that the speed measured from the image series is the maximum speed in the tube, the speed of the flow is recovered with an error of approximately 20%, due to the difficulty of choosing an optimal injection protocol.

4.9.2. Clinical

It has been seen that the proposed methodology to calculate the mean flow speed of a medium through front tracking is a feasible technique for simple and ideal flow situations. For the technique to be useful, it must be viable in realistic clinical cases. Although the results obtained from the study of a clinical case are not reliable at present, it is interesting to see how the algorithms tackle









4. BLOOD FLOW IN THE BRAIN

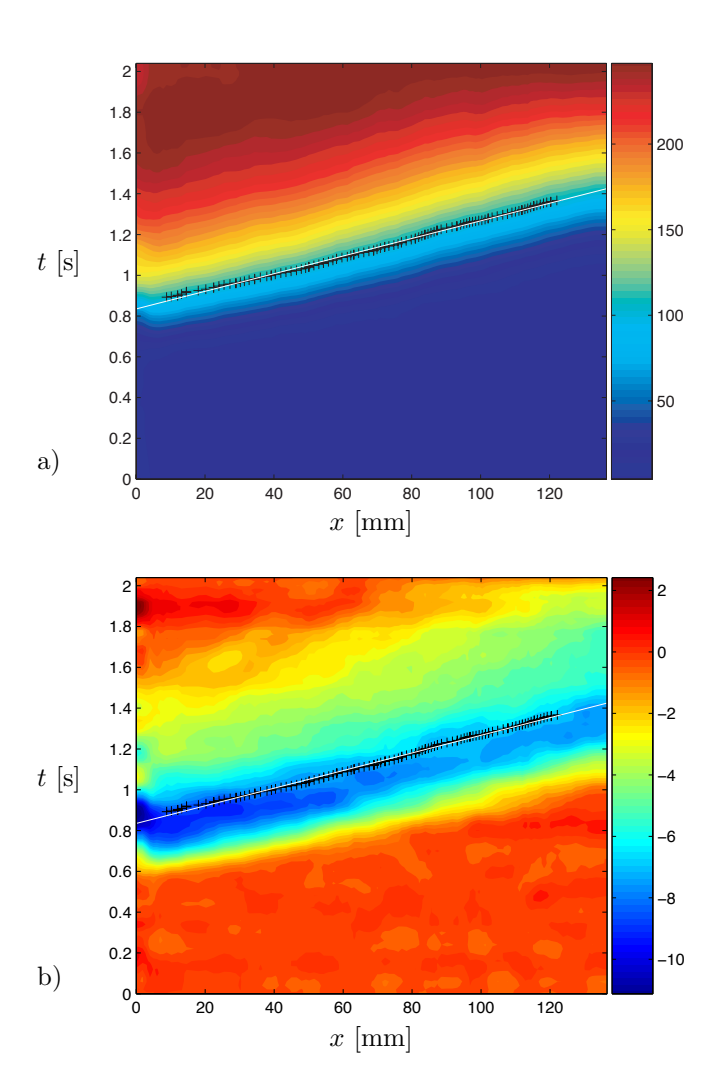


FIGURE 4.12. A two-dimensional contour map of a) the intensity during a 6-9 injection through a 4F catheter for flow A. In b), the gradient of the contour map is plotted. In both a) and b), a contrast intensity level of 100 is shown (+). A straight line is fitted to the data and plotted in white.

more complex morphologies. To this end, a clinical case of flow through an artery to an aneurysm and through vascular branching was studied.

In Figure 4.13, the contrast intensity was plotted versus time. Solid curves (—) signify clusters before the aneurysm, while dotted curves (\cdots) signify clusters after the aneurysm. The dashed curves (- - -) are clusters in the aneurysm. The contrast front is sharpest in the proximal region of the vessel tree. As









4.9. RESULTS

51

the contrast laden fluid travels through the vessel tree, it will diffuse in the direction of the flow both due to diffusion and to dynamic mixing mechanisms.

The pre-aneurysm curves seem to act as expected, as do the aneurysm curves. The location of the clusters in the aneurysm on the other hand raises some questions. The usual normal cross-sections of the vessel are here irregular pieces situated at unexpected positions in the aneurysm. The complex flow in the aneurysm coupled with the process of averaging values over the voxels in a cluster are the causes of significant uncertainty regarding the arrival of contrast at a certain position in the aneurysm.

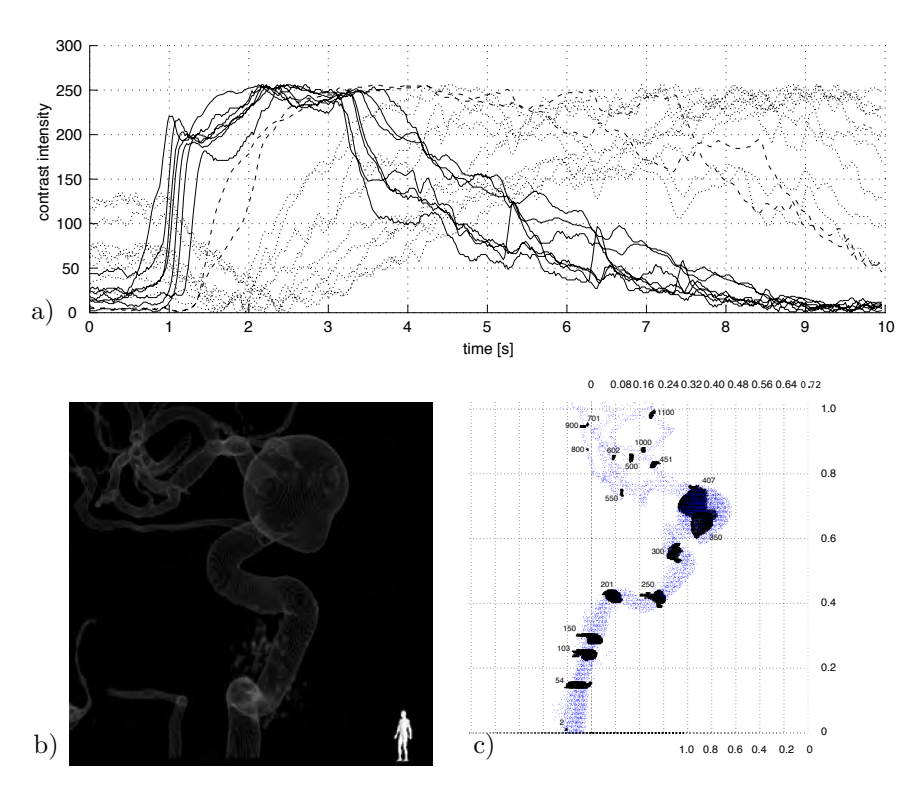


FIGURE 4.13. Time-intensity curves (a) for flow through an advanced clinical morphology. Solid curves (—) signify clusters before the aneurysm, while dotted curves (\cdots) signify clusters after the aneurysm. In b) and c), the reconstruction and studied clusters are presented.

In the images from the clinical trial, it can be observed that the intensity curves in the proximal vascular region shown in Figure 4.13 vary periodically. After the initial contrast bolus, pulsations of contrast are drawn forward with every beat of the heart, and arise either from entrainment areas around the catheter or from inside the end of it. These minor pulsations offer a number





"gunderhaegg" — 2006/4/27 — 14:21 — page 52 — #59





4. BLOOD FLOW IN THE BRAIN

of additional data sets that may be used to calculate flow properties. The amount of contrast connected with the mini-boli will also affect the flow in a lesser fashion allowing for a more accurate velocity prediction.

Further details concerning the experimental and clinical trials and practical implications of these theories are available in Paper 7.

4.10. Summary

From the results above, it is clear that the proposed methodology will provide reproducible mean flow characteristics for the tested idealized flow conditions. The calculated results give an estimated error interval of approximately $\pm 15\%$ for steady, laminar flow in a straight pipes. It is not improbable that this accuracy is applicable to the larger moderately tortuous vessels at the base of the cranium, or perhaps even in the brain. This opens for a practical tool that can be used to optimize therapy.

The injection protocol is of importance for the measurement accuracy. In the case of contrast front tracking, flow opacification is a primary clinical goal, while the time for which the flow is opacified is of lesser consequence. A train of short, concentrated injections would offer more data during the same trial while also affecting the flow to a lesser degree.

The algorithms are to be tested on phantom vasculature of increasing complexity. A series of experiments has been carried out on a U-bend, but these are as yet not analysed. Two additional geometries that would provide increasing complexity and with them characteristic flow complexity are serpentine and corkscrew geometries.









CHAPTER 5

Conclusions and outlook

5.1. Rotation

The effect of rotation on turbulent flow was probed both experimentally and via numerical simulations. Paper 1, Mårtensson et al. (2002), describes an experimental study of the pressure drop in a rotating rectangular duct for varying rotational rates and flow speeds. Previous studies of this kind performed by Dobner (1959), Johnston et al. (1972) and Rothe (1975) did not achieve the extreme rotation rates or flow speeds attained in this study. The experiments elucidated on the importance of the turbulent Ekman-like boundary layers for the pressure drop in rotating ducts. The experimental method in Paper 1 is explained thoroughly in Paper 4.

The size of the experimental set-up used was limited for practical reasons. This limitation in size brought about interesting questions concerning the degree of development of the flow. The reasoning in Paper 1 is based on the assumption of fully developed turbulent flow. For Paper 2, Mårtensson (2004) performed RANS computations of developing turbulent flow in a rotating duct, as well as a rotating channel, in order to obtain qualitative results concerning the effect of rotation on the development length for turbulent flow in a contained rotating system. Little work has been done concerning the study of developing flows in rotating ducts, although the case of developing flow in rotating channels has been studied experimentally by Koyama and Ohuchi (1985) and numerically by Dutzler et al. (2000). The computations have shown that the secondary flow induced in the duct has a significant effect on the characteristics of the flow and its development, shortening the length necessary for full development. The large number of turbulence models available in the EDGE package makes further studies with other models a tempting extension of this study.

The direct numerical simulation of turbulent flow in a rotating rectangular duct described in Paper 3 offers deepened insight into the effect of rotation on turbulent flow. The data made available through the DNS offers a considerable resource for the development of turbulence models.

The clear differences in the flows in rotating ducts and channels offer ideas for new studies. Grundestam et al. (2006) showed that rotating channel flow approaches a laminar profile at high rotation rates, leading us to ask what could be expected for the rotating duct case. One could conjecture that the





"gunderhaegg" — 2006/4/27 — 14:21 — page 54 — #61





54 5. CONCLUSIONS AND OUTLOOK

duct profile would approach an essentially two-dimensional profile with two very thin Ekman-like layers that would dominate the pressure drop in the duct.

5.2. Polymerase Chain Reaction

The computational studies presented in Papers 5 and 6 analyze the effect of rotation in of a novel PCR device. A model of the intricate boundary layer driven flow in the cone was developed and supported by computational simulations. The experimental data available gave further validity to the study.

PCR devices are designed to copy and analyze DNA specimens quickly and accurately. The goal of high throughput of many samples lends itself to configurations of a larger number of samples, but with smaller volumes. This type of *cone rack* with either 96 or 384 cones offers many new and challenging questions concerning positioning and temperature cycling protocols in order to ensure quick and accurate temperature homogenization and mixing.

5.3. Blood flow in the brain

In Paper 7, a method of obtaining quantitative flow information from high-speed x-ray registration of the injection of contrast agent in a blood vessel is tested experimentally in an idealized flow phantom. The method uses the three-dimensional data obtained from a rotational reconstruction of the vessel. The experiments show that although an acceptable quantitative agreement of mean flow speed may be obtained for simple flow morphologies, the results are sensitive to the injection protocol used.

A series of experiments are planned to examine several aspects of the injection protocol, such as the volume and temporal distribution of contrast medium injected into the vessel, synchronization of the injection with the pulsation of the blood and the positioning of the catheter at the point of injection in the main vessel.

A project has also been initiated to quantify the vortical strength of the flow in aneurysms, which together with the magnitude of the flow into the malformation could comprise valuable parameters to judge the risk of rupture in the aneurysm.









CHAPTER 6

Papers and author contributions

Paper 1

Mårtensson, G.E., Gunnarsson, J., Johansson, A.V. and Moberg, H. 2002 "Experimental investigation of a rapidly rotating turbulent duct flow" *Exp. Fluids*, **33**, pp. 482–487.

The experimental work studied in Paper 1, was performed by Gunnarsson (JG). The experimental data was examined and presented by Mårtensson (GM). The paper was written by GM and examined by Moberg (HM) and Johansson (AJ).

Paper 2

MÅRTENSSON, G.E., WALLIN, S. AND JOHANSSON, A.V. 2006 "A numerical study of developing turbulent flow in a rotating duct and a rotating channel", To be submitted.

The calculations in Paper 2 were initiated and performed by GM. Essential aid concerning the computational package was supplied by Stefan Wallin (SW). The evaluation of data was performed by GM with valuable comments by AJ and SW. The paper was written by GM with comments from AJ and SW.

Paper 3

MÅRTENSSON, G.E., BRETHOUWER, G. AND JOHANSSON, A.V. 2006 "Direct numerical simulation of rotating turbulent duct flow", Submitted to *Journal of Turbulence*.

The direct numerical simulation performed for Paper 3 was initiated by GM. The simulation code, as well as technical support, was supplied by Geert Brethouwer (GB). The data from the simulations were evaluated by GM, GB and AJ. The paper was written by GM and scrutinized by GB and AJ.

Paper 4

MÅRTENSSON, G.E. AND GUNNARSSON, J. 2004 "Details of experiments performed on rotating duct flow", Internal report, Department of Mechanics, KTH, Stockholm, Sweden.

Paper 4, which describes the experimental procedure used in Paper 1, was written by GM, while rebuilding the apparatus for complementary measurements.









6. Papers and author contributions

Paper 5

MÅRTENSSON, G., SKOTE, M., MALMQVIST, M., FALK, M., ASP, A., SVANVIK, N. AND JOHANSSON, A. 2006 "Rapid PCR amplification of DNA utilizing Coriolis effects", *Eur. Biophys. J.*, DOI 10.1007/s00249-006-0052-z.

The calculations that underly Paper 5 were initiated by GM and continued by Martin Skote (MS). Discussions were undertaken regularly with AJ, Mats Malmqvist (MM), Nicke Sandvik (NS) and later Allan Asp (AA). The experiments were performed by MM, NS, AA and Mats Falk (MF). Paper 5 was written by GM and MS with comments from AJ, AA and MM.

Paper 6

SKOTE, M., MÅRTENSSON, G.E. AND JOHANSSON, A.V. 2006 "Flow in a rapidly rotating cone-shaped PCR-tube", Submitted to *International Journal of Heat and Fluid Flow*.

The calculations that underly Paper 6 were initiated by GM and continued by Martin Skote (MS). Discussions were undertaken regularly with AJ, Mats Malmqvist (MM), Nicke Sandvik (NS) and later Allan Asp (AA). The experiments were performed by MM, NS, AA and Mats Falk (MF). Paper 6 was written by GM and MS with comments from AJ, AA and MM.

Paper 7

MÅRTENSSON, G.E., ANDERSSON, T., SÖDERMAN, M. AND JOHANSSON, A.V. 2006 "Cerebral arterial flow characteristics – analysis with 3D videodensitometry", Submitted to *Radiology*.

The experiments that lay the basis for Paper 7 were designed, built and performed by GM, with input from AJ, Michael Söderman (MS) and Tommy Andersson (TA). The Winflow package that reconstruct x-ray projections was written by Holger Schmitt (HS) at Philips Medical Systems. The data was evaluated by GM. The paper was written by GM, commented by AJ and severely edited by MS.









Acknowledgments

It's hard to believe that this thesis is actually here. While being very proud of myself, I will take a break from patting myself on the back to pay my respects to some of those who deserve varying degrees of praise and gratitude.

Naturally, I will begin with *Anna*, *Benjamin* and *Tyra*. In spite of a flexible schedule as a PhD student, many a long evening and busy weekend has been spent studying data files and analyzing plots. When you love what you do, it's wonderful to have something even better waiting for you at home.

I owe my advisor *Arne Johansson* a great debt of gratitude. With the patience and knowledge of Achaiah, he has accompanied me during this academic journey. He has inspired me to succeed, while allowing me to fail.

While working at Alfa Laval, I was constantly reminded of the virtues of humility with respect to knowledge and relationships by *Hans Moberg*.

Through my project at Karolinska University Hospital, I was fortunate enough to acquire even more role models. *Michael Söderman* and *Tommy Andersson* have instilled in me the importance of communication and accepting the possibility that we don't understand each other even when we think we do.

Anyone who knows me can tell you where I can be found every Friday morning between 8 and 9 am. To all of you at *sub rosa*,...thank you for almost six years of discussions concerning everything, and I mean everything!

Finally, I would like to thank my band of room mates, *Arnim, Jukka, Johan, Olof, and Linus* for so many things; for enduring my erratic comings and goings, for accepting my piles of articles, magazines, clothes and almost anything else, and for making coming to the department something I always looked forward to.









Bibliography

- Becker, E. 1972 "Chemically Reacting Flows", Ann. Rev. Fl. Mech., 4, pp. 155–194.
- Bruijns J. 2001 Shape from Voxels (Reference Manual). Philips Research Laboratories, Eidhoven, The Netherlands, 2001.
- Cebral, J.R., Castro, M.A., Appanaboyina, S., Putman, C.M., Millan, D. and Frangi, A.F. 2005 "Efficient Pipeline for Image-Based Patient-Specific Analysis of Cerebral Aneurysm Hemodynamics: Technique and Sensitivity", *IEEE Trans. Med. Im.*, **24**, pp. 457–467.
- Columbus, R.L., Helfer, J.L., Porte, J.J. and Wellman, J.A. 1990 "Temperature cycling cuvette" United States Patent 4,902,624.
- Cormack, A. M. 1963 "Representation of a Function by Its Line Integrals, with Some Radiological Applications", J. Applied Physics, 34, pp. 2722–2727.
- Cornelia, Z., Jürgens, H., Evertsz, C.J.G., Leppek, R., Peitgen, H.-O. and Klose, K.J. 1995 "Portal vein reconstruction based on topology", *Euro. J. Rad.*, **19**, pp. 96–100.
- Dobner, E. 1959 "Über den Strömungswiderstand in einem rotierenden Kanal", Dissertation, Technische Hochschule Darmstadt.
- Dutzler, G.K., Pettersson-Reif, B.A. and Andersson, H.I. 2000 "Relaminarization of turbulent flow in the entrance region of a rapidly rotating channel", *Int. J. of Heat and Fluid Flow*, **21**, pp. 49–57.
- Feldkamp, L.A., Davis, L.C., Kress, J.W. 1984 "Practical cone-beam algorithm", Journal of the Optical Society of America A, 1, pp. 612–619.
- Firmin, D.N., Nayler, G.L., Klipstein, R.H., Underwood, S.R., Rees, R.S. and Longmore, D.B. 1987 "In vivo validation of mr velocity imaging", *J. Comput. Assist. Tomogr.*, **11**, pp. 751–756.
- Gabe, I.T., Gault, J.H., Ross, J.Jr., Mason, D.T., Mills, C.J., Schillingford, J.P. and Braunwald, E. 1969 "Measurement of instantaneous blood flow velocity and pressure in conscious man with a catheter-tip velocity probe", Circulation, 40, pp. 603–614.
- Gavrilakis, S. 1992 "Numerical simulation of low-Reynolds-number turbulent flow through a straight square duct", *J. Fluid Mech.*, **244**, pp. 101–129.
- Grass, M., Koppe, R., Klotz, E., Op de Beek, J. and Kemkers, R. 1999 "3d reconstruction and imaging based on c-arm systems", *Medical & Biological Engineering & Computing*, **23**, pp. 311–321.









BIBLIOGRAPHY

59

- Grass, M., Koppe, R., Klotz, E., Proksa, R., Kuhn, M.H., Aerts, H., Op de Beek, J. and Kemkers, R. 1999 "Three-dimensional reconstruction of high contrast objects using c-arm image intensifier projection data", Computerized Medical Imaging and Graphics, 23, pp. 311–321.
- Greenspan, H.P. The Theory of Rotating Fluids, Cambridge University Press, 1968.
- Grundestam, O., Wallin, S. and Johansson, A.V. 2006 "Direct numerical simulations of rotating channel flow", Ph.D. thesis of Olof Grundestam, Dept. of Mech., Royal Inst. of Tech., Stockholm, Sweden, Paper 5, TRITA-MEK Technical report 2006:04.
- Halleen, R.M. and Johnston, J.P. 1967 "The influence of Rotation on Flow in a Long Rectangular Channel An Experimental Study", Ph.D. thesis, Stanford University, also Rep. MD-18, Thermosciences Div., Dept. of Mech. Engrg., Stanford University.
- Hermann, H., Knippschild, C. and Berka, A. 2004 "Ultrafast dna-amplification with a rapid pcr-system", BTi, November.
- Johnston, J.P., Halleen, R.M. and Lezius, D.K. 1972 "Effects of spanwise rotation on the structure of two-dimensional fully developed turbulent channel flow", J. Fluid Mech., 56, pp. 533–557.
- Koyama, H.S., Ohuchi, M. 1985 "Effects of Coriolis force on boundary layer development", Proceedings of the Fifth Symposium on Turbulent Shear Flows, Ithaca, New York, pp. 21.19–21.24.
- Luessenhop, A.J. and Spence, W.T. 1960 "Artificial embolization of cerebral arteries. Report of use in a case of arteriovenous malformation", JAMA, 172, pp. 1153-1155.
- Lumley, J. 20001 "Early work on fluid mechanics in the IC engine", Ann. Rev. Fl. Mech., 33, pp. 319–338.
- Leksell, L. 1951 "The stereotaxic method and radio surgery of the brain", Acta Chir. Scand., 102, pp. 316–319.
- Malmquist, M. 2004 "Homogenizing of small-volume mixtures by centrifugation and heating". United States Patent 6,783,993.
- Metcalfe, R. W. 2003 "The promise of computational fluid dynamics as a tool for delineating the rapeutic options in the treatment of aneurysms", $AJNR\ Am.\ J.\ Neuroradiol.,\ {\bf 24},\ {\rm pp.\ 553-554}.$
- Molyneux, A. et al. 2002 "International Subarachnoid Aneurysm Trial (ISAT) of neurosurgical clipping versus endovascular coiling in 2143 patients with ruptured intracranial aneurysms: a randomised trial", *Lancet*, **360**, pp. 1267–1274.
- Moniz, E. 1927 "L'encéphalographie artérielle, somn importance dans la localisation des tumeurs cérébrales", Rev. Neurol., 2, pp. 72–89.
- Mårtensson, G.E., Gunnarsson, J., Johansson, A. V. and Moberg, H. 2002 "Experimental investigation of a rapidly rotating turbulent duct flow", *Exp. Fluids*, **33**, pp. 482–487, DOI: 10.1007/s00348–002–0487–7.
- Mårtensson, G.E and Gunnarsson, J. 2004 "Details of experiments performed on rotating duct flow", Licentiate thesis of Gustaf Mårtensson, Dept. of Mechanics, Royal Inst. of Tech., Stockholm, Sweden, Paper 2, TRITA-MEK 2004:3.
- Mårtensson, G.E. 2006, "A numerical study of developing turbulent flow in a rotating duct and a rotating channel", Ph.D. thesis of Gustaf Mårtensson, Dept.









60 BIBLIOGRAPHY

- of Mechanics, Royal Inst. of Tech., Stockholm, Sweden, Paper 3, TRITA-MEK 2004:3.
- Newton, I. Philosophiae Naturalis Principia Mathematica, Royal Society, 1687.
- Nilsen, P.J. and Andersson, H.I. 1994 "Developing turbulent flow in a rotating channel", Int. J. of Heat and Fluid Flow, 15, pp. 100–103.
- Petersen, K.E., McMillan, W.A., Kovacs, G.T.A. and Young, S.J.1999 "Reaction vessel for heat-exchanging chemical processes", United States Patent 5,958,349.
- Pettersson Reif, B.A. and Andersson, H.I. 2003 "Turbulent flow in a rotating square duct: a modelling study", J. of Turbulence, 4, 012.
- Philip, J.R. 1970 "Flow in Porous Media", Ann. Rev. Fl. Mech., 2, pp. 177-204.
- Pile-Spellman, J.M., Baker, K.F., Liszczak, T.M., Sandrew, B.B., Oot, R.F., Debrun, G., Zervas, N.T. and Taveras, J.M. 1986 "High-flow angiopathy: cerebral blood vessel changes in experimental chronic arteriovenous fistula", AJNR Am J Neuroradiol., 7, pp. 811–815.
- Reyner, P. and Glover J. 1897 *Premiere Ventriculographie*, Recherches anatomichirurgicales au moyen de la radiographie II, pp. 580–585.
- Ristorcelli, J.R., Lumley, J.L. and Abid, R. 1995 "A rapid-pressure covariance representation consistent with the Taylor-Proudman theorem materially frame indifferent in the two-dimensional limit", *J. Fluid Mech.*, **292**, pp. 111–152.
- Rothe, P.H. 1975 "The effects of system rotation on seperation, reattachment and performance in two-dimensional diffusors", Ph.D. thesis, Stanford University, Dept. Mechanical Engineering.
- Saiki, R.K., Scharf, S., Faloona, F., Mullis, K. B., Horn, G. T., Erlich, H. A. and Arnheim, N. 1985 "Enzymatic Amplification of β -Globin Genomic Sequences and Restriction Site Analysis for Diagnosis of Sickle Cel Anemia", *Science*, **230**, pp. 1350–1354.
- Saiki, R. K., Gelfand, D. H., Stoffel, S., Scharf, S. J., Higuchi, R., Horn, G. T., Mullis, K. B. and Erlich, H. A. 1988 "Primer-Directed Enzymatic Amplification of DNA with a Thermostable DNA Polymerase", Science, 239, pp. 487–491.
- Schmiel, F.K., Huber, H., Neuhaus, K.L., and Spiller, P. 1978 "Densitometric measurements of coronary blood flow: methodological improvements", In B. J. Heintzen, H., editor, Roentgen video techniques for dynamic studies of structure and function of the heart and circulation, pages 49–55. Georg Thieme Publishers.
- Schmitt, H. 2000 "Feasibility study on the determination and visualization of the time-dependent distribution of contrast agent in cerebral vessel trees", Master's thesis, University of Heidelberg/University of Applied Sciences Heilbronn.
- Schmitt, H., Grass, M., Rasche, V., Schramm, O., Haehnel, S. and Sartor, K. 2002 "An x-ray-based method for the determination of the contrast agent propagation in 3-d vessel structures", *IEEE Transactions on Medical Imaging*, **21**, pp. 251–262.
- Schmitt, H., Grass, M., Suurmond, R., Köhler, T., Rasche, V., Hähnel, S. and Heiland, S. 2005 "Reconstruction of blood propagation in three-dimensional rotational x-ray angiography (3d-ra)", Computerized Medical Imaging and Graphics, 29, pp. 507–520.
- Settles, G.S. 2006 "Fluid mechanics and homeland security", Ann. Rev. Fl. Mech., 38, pp. 87–110.









BIBLIOGRAPHY

61

- Sjögren, T. and Johansson, A.V. 2000 "Development annud calibration of algebraic non-linear models for terms in the Reynolds stress transport equations", Phys. Fluids, 12, pp. 1554–1572.
- Smirnov, E.M. and Yurkin, S.V. 1983 "Fluid flow in a rotating channel of square section", Fluid Dyn., 18(6), pp. 850–855.
- Sorescu, G.P., Sykes, M., Weiss, D., Platt, M.O., Saha, A., Hwang, J., Boyd, N., Boo, Y.C., Vega, J.D., Taylor, W.R. and Jo, H. 2003 "Bone morphogenic protein 4 produced in endothelial cells by oscillatory shear stress stimulates an inflammatory response", *The Journal of Biological Chemistry*, **278**, pp. 311–328.
- Speziale, C.G., Sarkar, S. and Gatski, T.B. 1991 "Modelling the pressure-strain correlation of turbulence: an invariant dynamical systems approach", *J. Fluid Mech.*, **227**, pp. 245–272.
- Spiers, F. 1943 "Materials for depth dose measurement", *British Journal of Radiology*, **16**, pp. 90.
- Spiller, P., Schmiel, F.K., Politz, B. et al. 1983 "Measurements of systolic and diastolic flow rates in the coronary artery system by x-ray densitometry", *Circulation*, **68**, pp. 337–347.
- Steiner, L., Leksell, L., Greitz, T., Forster, D.M. and Backlund, E.O. 1972 "Stereotaxic radiosurgery for cerebral arteriovenous malformations. Report of a case." Acta Chir. Scand., 138, pp. 459–64.
- Stone, H.A., Stroock, A.D. and Ajdari, A. 2004 "Engineering flows in small devices", Ann. Rev. Fl. Mech., 36, pp. 381–411.
- Taylor, C.A. and Draney, M.T. "Experimental and computational methods in cardiovascular fluid mechanics", *Ann. Rev. Fl. Mech.*, **36**, pp. 197–231.
- Vanyo, J.P. Rotating Fluids in Engineering and Science, Dover Publ., Inc., New York, 2001, ISBN 0-486-41704-02.
- Walker, M.F., Souza, S.P. and Dumoulin, C.L. 1988 "Quantitative flow measurement in phase contrast mr angiography", J. Comput. Assist. Tomogr., 12, pp. 304–313
- Wallin, S. and Johansson, A.V. 2002 "Modelling streamline curvature effects in explicit algebraic Reynolds stress turbulence models", *Int. J. Heat and Fluid Flow*, **23**, pp. 721–730.
- Walter, P., McGahan, J.P. and Lantz, B.M.T 1986 "Absolute flow measurements using pulsed doppler us", *Radiology*, **159**, pp. 545–548.
- Watson J.D. and Crick F.H. 1953 "Molecular structure of nucleic acids; a structure for deoxyribose nucleic acid", *Nature*, **171**, pp. 737–738.
- Wittwer, C.T., Fillmore, G.C. and Hillyard, D.R. 1989 "Automated polymerase chain reaction in capillary tubes with hot air", *Nucleic Acids Research*, **17**, pp. 4353–4357.







"gunderhaegg" — 2006/4/27 — 14:21 — page 62 — #69





